

AD-A102 480

PHYSICAL DYNAMICS INC BELLEVUE WA
HELE-SHAW CELL EXPERIMENTS FOR SIMULATION OF STRUCTURES IN HIGH-ETC(U)
DEC 80 E J FREMOW
PD-NW-80-236R

F/6 20/9

DNA001-79-C-0132
NL

UNCLASSIFIED

DNA-5541F

1 OF 1

AD-A
102 480

END

DATE

FILED

8 81

DTIC

LEVEL

12

DNA 5541F

HELE-SHAW CELL EXPERIMENTS FOR SIMULATION OF STRUCTURES IN HIGH-ALTITUDE PLASMAS

Physical Dynamics, Inc.
P.O. Box 3027
Bellevue, Washington 98009

DTIC
AUG 5 1981

10 December 1980

Final Report for Period 1 October 1979-11 October 1980

CONTRACT No. DNA 001-79-C-0132

APPROVED FOR PUBLIC RELEASE;
DISTRIBUTION UNLIMITED.

THIS WORK SPONSORED BY THE DEFENSE NUCLEAR AGENCY
UNDER RDT&E RMSS CODE B322079464 S99QAXHC04118 H2590D.

Prepared for
Director
DEFENSE NUCLEAR AGENCY
Washington, D. C. 20305

81 8 05 009

AD A102480

AD A102480

Destroy this report when it is no longer
needed. Do not return to sender.

PLEASE NOTIFY THE DEFENSE NUCLEAR AGENCY,
ATTN: STTI, WASHINGTON, D.C. 20305, IF
YOUR ADDRESS IS INCORRECT, IF YOU WISH TO
BE DELETED FROM THE DISTRIBUTION LIST, OR
IF THE ADDRESSEE IS NO LONGER EMPLOYED BY
YOUR ORGANIZATION.



UNCLASSIFIED

SECURITY CLASSIFICATION OF THIS PAGE (When Data Entered)

19 REPORT DOCUMENTATION PAGE		READ INSTRUCTIONS BEFORE COMPLETING FORM	
1. REPORT NUMBER DNA 5541F	2. GOVT ACCESSION NO. AD-A102 480	3. RECIPIENT'S CATALOG NUMBER	
4. TITLE (and Subtitle) HELE-SHAW CELL EXPERIMENTS FOR SIMULATION OF STRUCTURES IN HIGH-ALTITUDE PLASMAS		5. TYPE OF REPORT & PERIOD COVERED Final report for period 1 Oct 79-11 Oct 80	
7. AUTHOR(S) Edward J. Fremouw		6. PERFORMING ORG. REPORT NUMBER PD-NW-80-236R	
9. PERFORMING ORGANIZATION NAME AND ADDRESS Physical Dynamics, Inc. P. O. Box 3027 Bellevue, Washington 98009		8. CONTRACT OR GRANT NUMBER(S) DNA 001-79-C-0132	
11. CONTROLLING OFFICE NAME AND ADDRESS Director Defense Nuclear Agency Washington, D.C. 20305		10. PROGRAM ELEMENT, PROJECT, TASK AREA & WORK UNIT NUMBERS Subtask 17 S99QAXHC041-18	
14. MONITORING AGENCY NAME & ADDRESS (if different from Controlling Office)		12. REPORT DATE 10 December 1980	
16. DISTRIBUTION STATEMENT (of this Report) Approved for public release; distribution unlimited.		13. NUMBER OF PAGES 60	
17. DISTRIBUTION STATEMENT (of the abstract entered in Block 20, if different from Report)		15. SECURITY CLASS (of this report) UNCLASSIFIED	
18. SUPPLEMENTARY NOTES This work sponsored by the Defense Nuclear Agency under RDT&E RMSS Code B322079464 S99QAXHC04118 H2590D.		15a. DECLASSIFICATION DOWNGRADING SCHEDULE N/A	
19. KEY WORDS (Continue on reverse side if necessary and identify by block number) Striations Rayleigh-Taylor Instability Magnetohydrodynamic Convection Flow Visualization			
20. ABSTRACT (Continue on reverse side if necessary and identify by block number) The magnetohydrodynamic (MHD) equations that describe the motion of a tenuous plasma in a uniform magnetic field are mathematically analogous to the hydrodynamic equations describing two-dimensional flow of an incompress- ible fluid. As a consequence, one can construct a laboratory analogue of MHD phenomena involved in the structuring of high-altitude plasma clouds on scales that lead to radiowave scintillation. A simple laboratory tool for			

DD FORM 1 JAN 73 1473

EDITION OF 1 NOV 65 IS OBSOLETE

UNCLASSIFIED 393400
SECURITY CLASSIFICATION OF THIS PAGE (When Data Entered)

UNCLASSIFIED

SECURITY CLASSIFICATION OF THIS PAGE(When Data Entered)

visualizing the relevant dynamics is the Hele-Shaw cell, which consists of two pieces of plate glass between which appropriate fluids are constrained to undergo two-dimensional flow. Two fluids of different density but equal kinematic viscosity are placed in a Hele-Shaw cell with a uniform boundary between them, and the cell is oriented vertically with gravity acting across the boundary. Within a few seconds, the boundary becomes structured under the influence of the Rayleigh-Taylor instability, which then may be studied well into its nonlinear regime.

In the dynamic analogue that ensues, the fluid density and velocity represent respectively the plasma density and convective velocity (in the $E \times B$ regime), the fluid stream function represents the electrostatic potential, and the gravitationally driven free-fall velocity in the cell represents the gravitationally assisted neutral-wind velocity in the ionosphere. In this report, the mathematical underpinnings of the analogue are reviewed; they are found quite firm for scales in excess of about 100 meters in the nighttime equatorial F layer, subject to one untested assumption.

Under this contract, a Hele-Shaw cell capable of providing repeatable experimental conditions necessary for systematic study of Rayleigh-Taylor structuring was built and several exploratory experimental runs were made. Difficulties were encountered with a densitometer used for data preparation, but useable results were obtained. The cell and laboratory procedures produced sufficient photographic signal-to-noise ratios to demonstrate that definitive studies of the spatial spectrum of Rayleigh-Taylor structure are possible in the spectral regime for which the presently developed mathematical analogue is valid.

All spectra obtained show a clear break between a white-noise regime and a power-law tail, interpreted as an outer scale. All experimental runs analyzed reveal an increase in the outer scale near the original fluid interface during their tens-of-seconds duration. Photographic records suggest rather nonuniform spatial statistics as a function of distance from the original interface. This report presents results on evolution of the outer scale near the original interface, suggests means for probing its control, and poses other spatial-statistical questions that could yield to Hele-Shaw analysis.

UNCLASSIFIED

SECURITY CLASSIFICATION OF THIS PAGE(When Data Entered)

TABLE OF CONTENTS

<u>Section</u>	<u>Page</u>
LIST OF ILLUSTRATIONS -----	2
LIST OF TABLES -----	3
I INTRODUCTION -----	5
II THEORETICAL CONSIDERATIONS -----	6
A. FIRST POINT OF ANALOGY -----	6
B. ELECTRODYNAMICS IN THE ANALOGY -----	10
C. SUMMARY OF THEORETICAL RESULTS -----	19
III EXPERIMENTAL APPARATUS AND PROCEDURES -----	22
A. THE CELL -----	22
B. LABORATORY PROCEDURES -----	24
IV ANALYSIS PROCEDURES -----	29
A. DENSITOMETRY -----	29
B. SPECTRAL ANALYSIS -----	37
V RESULTS -----	40
VI CONCLUSION -----	46
REFERENCES -----	50

Accession For	
NTIS GPO&I	<input checked="" type="checkbox"/>
DTIC T B	<input type="checkbox"/>
Unannounced	<input type="checkbox"/>
Justification	
By _____	
Distribution/	
Availability Codes	
Dist	Special
A	

LIST OF ILLUSTRATIONS

<u>Figure</u>		<u>Page</u>
1	The Hele-Shaw cell (white central rectangle) in its frame and pivot mount, showing light box (large off-white rectangle), clocks, and overall size -----	23
2	Data frames showing Rayleigh-Taylor unstable fluid interface without counteraction of cell bulge (left) and with counteraction by control of hydrostatic head (right) -----	26
3	Densitometer scans across stable fluid interface (top) and structured interchange region (bottom) -----	28
4	Nine data frames from Run #21, performed 10 October 1980 ----	30
5	Calibrated densitometer scans across pre-instability interface (top) and upper portion of structured interchange region (bottom) in Run #21 -----	33
6	Densitometer scans across the center of the interchange region at 6 times in Run #21 -----	35
7	Two densitometer scans across a photographic step tab, showing different bias and noise-fluctuation levels -----	36
8	Power spectra of the six densitometer scans shown in Figure 6, together with best-fit analytical spectra of the form given in Eq. (58) -----	38
9	Spectra from six sequential data frames of run #7, each from a scan through the middle of the structured region, and best-fit cutoff power laws -----	41
10	Densitometer scans (left) and corresponding spectra for Hele-Shaw Run #44 by Thomson -----	42
11	Evolution of the outer scale, L , in our runs #7 and #21 and Thomson's run #44 -----	44
12	In-situ plasma scan (bottom) and corresponding spectrum (top) obtained in the pre-midnight, bottomside, equatorial F layer (after Basu and Basu, 1978). Smooth curve in top panel is best fit of Eq. (58) to experimental spectrum -----	48

LIST OF TABLES

<u>Table</u>		<u>Page</u>
1	Pertinent Assumptions and Approximations -----	19
2	Mathematical Analogy -----	20
3	Analagous Parameters -----	20
4	Observed Morphology -----	46

I. INTRODUCTION

For about a decade, it has been known that there is a direct mathematical analogy between the motion and structuring of a variable-density plasma embedded in a magnetic field, in the low collision-frequency regime, and the motion and structuring of a variable-density, incompressible fluid embedded in a resistive medium (Thomson, 1970). Comparison of the structures that develop across magnetic field lines in high-altitude barium-ion clouds, under the influence of the gradient-drift plasma instability, with those that develop in fluid released in a Hele-Shaw cell, under the influence of the Rayleigh-Taylor instability, lends credence to the analogy.

Thomson's analogue and the experimental evidence for its validity offer a relatively inexpensive way to investigate some aspects of high-altitude magnetoplasma structures that can disrupt performance of radars and communication systems by means of radiowave scintillation. This report summarizes first attempts to exploit the analogue to establish certain characteristics of the spatial spectrum of such structures.

Work on the contract has shown that the Hele-Shaw technique is quite a useful tool for characterizing the spectrum at scales larger than about 100 m in the topside ionospheric F layer. The one-dimensional spectrum found is well characterized by a cutoff power law, and the Hele-Shaw technique reveals dynamically the evolution of its outer-scale cutoff.

The work reported herein included a review of Thomson's theoretical development and early Hele-Shaw experiments and, more recently, construction of an improved cell and performance of several experimental runs in it. Theoretical considerations are presented in Section II. Section III provides a description of the new cell, together with the laboratory and data-recording techniques employed for experimental runs in it. Procedures for data analysis, including a nagging hardware problem, are described in Section IV. Results and initial conclusions regarding the evolution of fluid (and magnetoplasma) structures are presented in Section V, along with suggestions for broader exploitation of the Hele-Shaw technique.

II. THEORETICAL CONSIDERATIONS

A. FIRST POINT OF ANALOGY

In order to provide a sound basis for applying the Hele-Shaw analogue, a detailed review of the MHD equations whose solution would describe the evolution of plasma structure in the ionosphere was undertaken, along with a review of the simpler corresponding hydrodynamic equations. In an effort to illuminate all important assumptions and approximations that might be required in developing the analogue, the rather general approach taken by Thomson (1970) was followed. In this section, we discuss the momentum equations, starting with the following ion and electron equations written in the earth frame:

$$nm_i \frac{d\vec{U}_i}{dt} = -\nabla P_i + en[\vec{E} + (\vec{U}_i \times \vec{B})] + nm_i \vec{g} - nm_i \nu_{in} (\vec{U}_i - \vec{V}) - m_e \nu_{ie} \frac{\vec{J}}{e} \quad (1)$$

$$nm_e \frac{d\vec{U}_e}{dt} = -\nabla P_e - en[\vec{E} + (\vec{U}_e \times \vec{B})] + nm_e \vec{g} - nm_e \nu_{en} (\vec{U}_e - \vec{V}) + m_e \nu_{ie} \frac{\vec{J}}{e} \quad (2)$$

where $\frac{d}{dt}$ stands for the convective derivative, and where

- n = plasma number density
 - $m_{i,e}$ = ion or electron mass
 - $\vec{U}_{i,e}$ = ion or electron velocity
 - \vec{V} = neutral-wind velocity
 - $P_{i,e}$ = ion or electron pressure
 - e = elementary charge
 - \vec{E} = electric field
 - \vec{B} = magnetic induction
 - \vec{g} = gravitational acceleration
 - ν_{in} = ion-neutral collision frequency
 - ν_{en} = electron-neutral collision frequency
 - ν_{ie} = ion-electron collision frequency
- and $\vec{J} = ne(\vec{U}_i - \vec{U}_e) =$ current density.

The beginning assumptions, then, include local neutrality (all relevant distances \gg Debye length), a single ion species of charge e , and infinitely heavy neutral particles (which can be accounted for in evaluating ν_{in}).

We proceed to the first important equation of the analogue by adding Eqs. (1) and (2) to obtain

$$nM \frac{d\vec{U}}{dt} = -\nabla P_p + (\vec{J} \times \vec{B}) + nM\vec{g} + nMv_n \vec{V} - n(m_i v_{in} \vec{U}_i + m_e v_{en} \vec{U}_e) \quad (3)$$

where we have defined

$$M = m_i + m_e \approx m_i$$

$$\vec{U} = \frac{m_i \vec{U}_i + m_e \vec{U}_e}{M} \approx \vec{U}_i$$

$$P_p = P_i + P_e \approx 2P_e \approx 2P_i$$

$$\text{and } v_n = \frac{m_i v_{in} + m_e v_{en}}{M} \approx v_{in}$$

Manipulation of the last term in Eq. (3), without approximation, yields

$$nM \frac{d\vec{U}}{dt} = -\nabla P_p + (\vec{J} \times \vec{B}) + nM\vec{g} + nMv_n (\vec{V} - \vec{U}) + \frac{m_i m_e}{M} v_d \frac{\vec{J}}{e} \quad (4)$$

$$\text{where } v_d = v_{en} - v_{in} \approx v_{en}$$

But since $m_e \ll m_i$, v_d while \vec{U}_e and \vec{U}_i are comparable and v_d is of similar order to v_n (although somewhat larger), we ignore the current term in Eq. (4). We then invoke Ampere's law in the electrostatic approximation, as follows:

$$\nabla \times \vec{B} = \mu_0 \vec{J} + \frac{1}{c^2} \frac{\partial \vec{E}}{\partial t} \approx \mu_0 \vec{J} \quad (5)$$

where μ_0 = magnetic permeability of free space.

Accordingly, we have

$$\vec{J} \times \vec{B} = \frac{(\nabla \times \vec{B}) \times \vec{B}}{\mu_0} = \frac{-\nabla B^2}{2\mu_0} + \frac{(\vec{B} \cdot \nabla) \vec{B}}{\mu_0} = \frac{-\nabla_{\perp} B^2}{2\mu_0} \quad (6)$$

or, for a magnetic field uniform in its own direction,

$$\vec{J} \times \vec{B} = \frac{\nabla_{\perp} B^2}{2\mu_0} \quad (7a)$$

$$= \nabla P_m \quad (7b)$$

where $P_m = \frac{B^2}{2\mu_0}$ is the magnetic pressure. With these further modest restrictions, Eq. (4) becomes

$$nM \frac{d\vec{U}}{dt} = -\nabla P + nM\vec{G} - nMv_n \vec{U} \quad (8)$$

where $P = P_p + P_m =$ the total pressure
 and $\vec{G} = \vec{g} + v_n \vec{V} =$ the acceleration due to gravity and the neutral wind. Alternatively, we may ignore gradients and motions parallel to the magnetic field and write

$$nM \frac{d\vec{U}_\perp}{dt} = -\nabla_\perp P + nM\vec{G}_\perp - nMv_n \vec{U}_\perp \quad (9)$$

Eqs. (8) and (9) are very similar to the Navier-Stokes equation for an incompressible fluid acted on by gravity, which is (cf. Lamb, 1945, Eq. 328-2) as follows:

$$\rho \frac{d\vec{U}}{dt} = -\nabla p + \rho \vec{g} + \frac{1}{3} \mu \nabla(\nabla \cdot \vec{u}) + \mu \nabla^2 \vec{u} \quad (10)$$

(incompressibility)

where $\vec{u} =$ fluid velocity

$\rho =$ mass density

$p =$ hydrostatic pressure

$\mu =$ viscosity.

To obtain an equivalence, we must investigate the final term in Eq. (10) in the Hele-Shaw-cell configuration.

A Hele-Shaw cell is simply two pieces of plate glass separated by a very small gap of dimension d , between which fluid is constrained to undergo two-dimensional flow. In the analogue, the magnetic-field direction corresponds to the interplate-gap direction. Since there is no motion across the gap, the pressure and gravity terms in that direction balance, and Eq. (10) is two-dimensional, as follows:

$$\frac{d\vec{u}_\perp}{dt} = -\frac{\nabla_\perp p}{\rho} + \vec{g}_\perp + \eta \nabla^2 \vec{u}_\perp \quad (11)$$

where $\eta = \frac{\mu}{\rho}$ is the kinematic viscosity. Further, the steady-flow approximation is well satisfied both in the field and in the laboratory, so Eq. (11) gives approximately

$$\nabla^2 \vec{u}_\perp = \frac{\nabla_\perp p - \rho \vec{g}_\perp}{\eta} \quad (12)$$

For a small gap dimension, d , we suppose that $\nabla_\perp^2 \vec{u}_\perp \rightarrow \nabla^2 \vec{u}_\perp \hat{=} \frac{\partial^2 \vec{u}_\perp}{\partial z^2}$, so Eq. (12) approximates

$$\frac{\partial \vec{u}_1}{\partial z} = \frac{\frac{\nabla_{\perp} P}{\rho} - \vec{g}_1}{\eta} \quad (13)$$

For constant kinematic viscosity, which we impose on our experimental fluids, we can write

$$\frac{\partial}{\partial z} \left(\frac{\frac{\nabla_{\perp} P}{\rho} - \vec{g}_1}{\eta} \right) = \frac{1}{\eta} \left[\frac{1}{\rho} \left(\frac{\partial^2 p}{\partial x^2} + \frac{\partial^2 p}{\partial y^2} - \frac{\nabla_{\perp} P}{\rho} \right) \frac{\partial \rho}{\partial z} \right] \quad (14)$$

and, from the balance of forces across the gap, we have

$$\frac{\partial p}{\partial z} = -\rho g_z \quad (15)$$

so

$$\frac{\partial}{\partial z} \left(\frac{\frac{\nabla_{\perp} P}{\rho} - \vec{g}_1}{\eta} \right) = \frac{1}{\eta} \left[\frac{1}{\rho} (g_z \nabla_{\perp} \rho) - \frac{\nabla_{\perp} P}{\rho^2} \frac{d\rho}{dz} \right] \quad (16)$$

For a vertically oriented cell, $g_z = 0$. If, also, we can ignore any density variation across the gap, then, the right-hand side of Eq. (13) is independent of z , and we can integrate to obtain

$$\vec{u}_1 = \left(\frac{\frac{\nabla_{\perp} P}{\rho} - \vec{g}_1}{2\eta} \right) z^2 + Bz + A \quad (17)$$

where A and B are to be evaluated from the boundary conditions at $z = 0$ and $z = d$, respectively. Denoting the slip velocity at the boundaries by u_s , we obtain the following cross-gap velocity profile:

$$\vec{u}_1 = \vec{u}_s + \left(\frac{\frac{\nabla_{\perp} P}{\rho} - \vec{g}_1}{2\eta} \right) (z^2 - zd) \quad (18)$$

which has the value

$$\vec{u}_c = \vec{u}_s - \frac{d^2}{8} \left(\frac{\frac{\nabla_{\perp} P}{\rho} - \vec{g}_1}{\eta} \right) \quad (19)$$

at the gap center.

Under the foregoing conditions, then,

$$\nabla^2 \vec{u}_1 = \frac{8}{d^2} (\vec{u}_c - \vec{u}_s) \quad (20)$$

and, for zero slip velocity, Eq. (11) becomes

$$\frac{d\vec{u}_1}{dt} = -\frac{\nabla_{\perp} p}{\rho} + \vec{g}_1 - \frac{8\eta}{d^2} \vec{u}_1 \quad (21)$$

where we have dropped the distinction between \vec{u}_1 and its maximum value, \vec{u}_c . Rewriting Eqs. (9) and (21), we have, for the plasma and cell fluid, respectively,

$$\frac{d\vec{U}_1}{dt} = \frac{-\nabla_{\perp} P}{nM} + \vec{G}_1 - \nu \nabla^2 \vec{U}_1 = 0 \quad (22a)$$

and

$$\frac{d\vec{u}_1}{dt} = \frac{-\nabla_{\perp} p}{\rho} + \vec{g}_1 - \frac{8\eta}{d^2} \vec{u}_1 = 0 \quad (22b)$$

where η is the kinematic viscosity, $\frac{\mu}{\rho}$.

Equations (22a and b) disclose the first point of analogy between the Hele-Shaw fluid and the magnetoplasma. They are acted upon respectively by hydrostatic pressure and magnetoplasma pressure (both gas-dynamic and magnetic); gravity drives the instability in the cell as can the gravitationally assisted neutral wind in the ionosphere, and scaled kinematic viscosity in the cell plays the roll of the ion-neutral collision frequency in setting up a drag force.

B. ELECTRODYNAMICS IN THE ANALOGY

While Eqs. (22a and b) do indeed suggest an analogy between Hele-Shaw fluids and magnetoplasmas of interest, the very important electrostatics of the former are quite hidden in the magnetic-pressure term of Eqs. (7, 8, and 22a). To bring them out, Thomson (1970) followed the procedure of considering electron and ion dynamics in detail to obtain relationships between the density, \vec{J} , of electric current flowing in the plasma and the plasma's convective velocity, \vec{U}_1 . Thus, if instead of adding Eqs. (1) and (2), we subtract them after dividing them respectively by nm_i and nm_e , we get

$$\frac{1}{ne} \frac{d\vec{J}}{dt} = \frac{-m_e \nabla P_i + m_i \nabla P_e}{nm_i m_e} + e \left[\frac{M\vec{E}}{m_i m_e} + \frac{(m_e \vec{U}_i + m_i \vec{U}_e)}{m_i m_e} \times \vec{B} \right] \quad (23)$$

$$+ v_{en} \vec{U}_e - v_{in} \vec{U}_i - v_d \vec{V} - \left(1 + \frac{m_e}{m_i}\right) v_{ie} \frac{\vec{J}}{ne} .$$

Manipulating various terms and defining

$$v_m = \frac{m_i v_{en} + m_e v_{in}}{M} + \frac{M}{m_i} v_{ie} = v_{en} + v_{ie} ,$$

but introducing no approximation, we obtain

$$\frac{1}{ne} \frac{d\vec{J}}{dt} = \frac{m_i \nabla P_e - m_e \nabla P_i}{nm_i m_e} + \frac{eM}{m_i m_e} \left[\vec{E} + (\vec{U} \times \vec{B}) \right] - \frac{(m_i - m_e)}{nm_i m_e} (\vec{J} \times \vec{B})$$

$$+ v_d (\vec{U} - \vec{V}) - \frac{v_m \vec{J}}{ne} . \quad (24)$$

On all time scales of interest, we may ignore electron acceleration, so the left-hand side above approximates $\frac{d\vec{U}_i}{dt}$ while that of Eq. (4) approximates $nm \frac{d\vec{U}_i}{dt}$. Scaling and equating the right-hand sides and performing some manipulations, while applying only the innocuous approximation $m_e^2 \ll m_i^2$, we obtain

$$\frac{m_e}{M} \frac{v_m}{ne} \vec{J} + \frac{\vec{J} \times \vec{B}}{nM} = \frac{e}{m_i} \left[\vec{E} + (\vec{U} \times \vec{B}) \right] + \frac{m_e}{M} (v_d + v_n) (\vec{U} - \vec{V}) - \frac{m_e}{M} (\vec{F}_p + \vec{G}_p) \quad (25)$$

where we have defined

$$\vec{F}_p = \frac{\nabla P_i}{nm_i} - \frac{\nabla P_e}{nm_e} \approx \frac{-\nabla P_e}{nm_e}$$

$$\text{and } \vec{G}_p = \vec{g} - \frac{\nabla P}{nm_i} \approx \vec{g} - \frac{\nabla P}{nm_i} .$$

Equation (25) is valid even for accelerating ion flow. To proceed with our case of interest, we make the steady-flow approximation, which is valid for subsonic flow and/or moderate-to-large plasma-density gradients. With both electron and ion acceleration neglected, we may set the left-hand side of Eq. (24) to zero and solve for the plasma velocity, \vec{U} , as follows:

$$\vec{U} = \vec{V} + \frac{\vec{g}}{v_n} - \frac{\nabla P_p}{nMv_n} + \frac{m_i m_e v_d}{M^2 v_n} \frac{\vec{J}}{ne} + \left(\frac{\vec{J}}{ne} \times \frac{\vec{\omega}_c}{v_n} \right) \quad (26)$$

where we have defined the gyro frequency

$$\vec{\omega}_c = \frac{e\vec{B}}{M}.$$

Inserting Eq. (26) into Eq. (25) and performing some vector manipulations, we obtain

$$\begin{aligned} & \left(\frac{m_i m_e}{Mne^2} v_m + \frac{M\omega_c^2}{ne^2 v_n} \right) \vec{J} - \frac{M\omega_c^2}{ne^2 v_n} J_{\parallel} \hat{z} + \frac{m_i}{ne^2} \left[1 - \frac{m_e}{M} \left(1 + 2 \frac{v_d}{v_n} \right) \right] (\vec{J} \times \vec{\omega}_c) \\ & = \left[\vec{E} + \frac{M}{e} (\vec{V} \times \vec{\omega}_c) \right] + \frac{m_i m_e}{Me} \left(\frac{v_d}{v_n} \vec{G}_p - \vec{F}_p \right) + \frac{M}{e} \left(\vec{G}_p \times \frac{\vec{\omega}_c}{v_n} \right) \end{aligned} \quad (27)$$

where \hat{z} is a unit vector in the direction of the magnetic field and J_{\parallel} is the magnitude of field-aligned current density.

The right-hand side of Eq. (27) may be thought of as an equivalent electric field, \vec{E} , driving the currents appearing on the left-hand side. Defining also

$$r_1 = \frac{m_i m_e}{Mne^2} v_m$$

$$r_2 = \frac{M\omega_c^2}{ne^2 v_n}$$

$$r_3 = \frac{m_i}{ne^2} \left[1 - \frac{m_e}{M} \left(1 + 2 \frac{v_d}{v_n} \right) \right] \omega_c$$

we may write Eq. (27) as

$$(r_1 + r_2) \vec{J} - r_2 J_{\parallel} \hat{z} + r_3 (\vec{J} \times \hat{z}) = \vec{\epsilon} ,$$

which may be solved for the vector current in terms of the equivalent driving field and the Pederson, Hall, and parallel conductivities as follows:

$$\vec{J} = \sigma_p \vec{\epsilon}_{\perp} + \sigma_H \frac{\vec{\omega}_c \times \vec{\epsilon}_{\perp}}{\omega_c} + \sigma_{\parallel} \epsilon_{\parallel} \hat{z} \quad (28)$$

where

$$\sigma_p = \left[(r_1 + r_2) + \frac{r_3^2}{(r_1 + r_2)} \right]^{-1} \approx \frac{ne^2}{M} \frac{v_n}{\omega_c^2} \left[\frac{1}{1 + (v_n/\omega_c)^2} \right]$$

$$\sigma_H = \frac{r_3}{r_1 + r_2} \sigma_p \approx \frac{v_n}{\omega_c} \sigma_p$$

$$\text{and } \sigma_{\parallel} = r_1^{-1} \approx \frac{ne^2}{m_e v_m}$$

The approximation in the conductivity definitions holds for $\frac{m_e}{m_i} \frac{v_m v_n}{\omega_c^2} \ll 1$ and therefore is valid so long as $(v_{en} + v_{ie})v_{in}$ is not $\gg \omega_c^2$.

From the continuity equation for charge density under either the electro-static or local-neutrality approximations, both of which were invoked in developing the momentum equation, we get

$$\nabla \cdot \vec{J} = 0 \quad (29)$$

Combining Eqs. (28) and (29) yields

$$\nabla_{\perp} \cdot (\sigma_p \vec{\epsilon}_{\perp}) + \nabla_{\perp} \cdot \left(\sigma_H \frac{\vec{\omega}_c \times \vec{\epsilon}_{\perp}}{c} \right) + \nabla_{\parallel} \cdot \sigma_{\parallel} \vec{\epsilon}_{\parallel} = 0 \quad (30)$$

Inserting the approximate forms for \vec{F}_p and \vec{G}_p into the definition of $\vec{\epsilon}$ and invoking $\frac{m_i}{m_e} \gg \frac{v}{v_{in}}$ $\gg 1$, we find

$$\vec{\epsilon} = \left[\vec{E} + \frac{M}{e} (\vec{V} \times \vec{\omega}_c) \right] + \frac{\nabla P_e}{ne} + \left(\frac{M}{e} \vec{g} - \frac{\nabla P_p}{ne} \right) \times \frac{\vec{\omega}_c}{v_n}. \quad (31)$$

Now employing Faraday's law in the magnetostatic approximation, we express \vec{E} in terms of a scalar potential, ϕ , and write

$$\vec{\epsilon} = \left[-\nabla\phi' + \frac{M}{e} (\vec{V} \times \vec{\omega}_c) \right] + \left(\frac{M}{e} \vec{g} - \frac{\nabla P_p}{ne} \right) \times \frac{\vec{\omega}_c}{v_n} \quad (32)$$

or

$$\vec{\epsilon} = -\nabla\phi' + (\vec{V}_f \times \vec{B}) \quad (33)$$

where we have defined

$$\nabla\phi' = \nabla\phi - \frac{\nabla P_e}{ne}$$

$$\text{and } \vec{V}_f = \vec{V} + \frac{1}{v_n} \left(\vec{g} - \frac{\nabla P_p}{nM} \right).$$

With these definitions, the current divergence equation takes the form of the following potential equation:

$$\begin{aligned} \nabla_{\parallel} \cdot (\sigma_{\parallel} \nabla_{\parallel} \phi') + \nabla_{\perp} \cdot (\sigma_p \nabla_{\perp} \phi') + \frac{v_n}{\omega_c} \nabla_{\perp} \cdot \left(\sigma_p \frac{\vec{\omega}_c \times \nabla_{\perp} \phi'}{\omega_c} \right) \\ = \frac{M}{e} \nabla_{\perp} \cdot \left[\sigma_p (\vec{V}_f \times \vec{\omega}_c) + \frac{v_n}{\omega_c} \sigma_p \frac{\vec{\omega}_c \times (\vec{V}_f \times \vec{\omega}_c)}{\omega_c} \right]. \end{aligned} \quad (34)$$

A series of vector manipulations without approximation leads to

$$\begin{aligned} \nabla_{\parallel} \cdot (\sigma_{\parallel} \nabla_{\parallel} \phi') + \nabla_{\perp} \cdot (\sigma_p \nabla_{\perp} \phi') - \frac{v_n}{\omega_c} \left[\nabla_{\perp} \sigma_p \cdot \left(\nabla_{\perp} \phi' \times \frac{\vec{\omega}_c}{c} \right) \right] \\ = \nabla_{\perp} \cdot \left[\sigma_p \left(\vec{f} + \vec{f} \times \frac{\vec{\omega}_c}{v_n} \right) \right] \end{aligned} \quad (35)$$

where we have defined

$$\vec{f} = \frac{M}{e} \nu \vec{V}_f = \frac{M}{e} \left[\nu \vec{V} + \left(\vec{g} - \frac{\nu \vec{p}}{nM} \right) \right].$$

In the same $m_i \gg m_e$ approximation, Eq. (26) for the plasma velocity becomes

$$\vec{U} = \vec{V}_f + \frac{m_e}{M} \frac{\nu en}{\nu_{in}} \frac{\vec{J}}{ne} + \left(\frac{\vec{J}}{ne} \times \frac{\vec{\epsilon}_c}{\nu_n} \right). \quad (36)$$

If the current is expanded in terms of the equivalent driving field, $\vec{\epsilon}$, and the three component conductivities, σ , and then Eq. (34) is inserted, a rather complicated expression for \vec{U} results. It may be manipulated, however, and without introducing any new approximation, broken into the following components parallel and perpendicular to the magnetic field:

$$U_{||} = (V_f)_{||} + \frac{e}{m_e} \frac{\nu en}{\nu_{in} \nu_m} \nu_{||} \phi' \quad (37a)$$

$$\vec{U}_{\perp} = \left[\frac{-\nabla_{\perp} \phi' \times \vec{B}}{B^2} + \frac{\nu n}{\omega_c} \left(\vec{V}_f \times \frac{\vec{B}}{B} \right) \right] + \left[\frac{\nu n}{\omega_c} \left(\frac{-\nabla_{\perp} \phi'}{B} \right) + \frac{\nu n^2}{\omega_c^2} (\vec{V}_f)_{\perp} \right]. \quad (37b)$$

In the regime $\nu_n \gg \omega_c$, then, we have for the perpendicular velocity

$$\vec{U}_{\perp} = \frac{-\nabla_{\perp} \phi' \times \vec{B}}{B^2} + \frac{\nu n}{\omega_c} \left(\vec{V}_f \times \frac{\vec{B}}{B} \right). \quad (38)$$

In the same regime, Eq. (35), which expresses the fact that the current is divergence-free, comprises

$$\nabla_{||} \cdot (\sigma_{||} \nabla_{||} \phi') = 0 \quad (39)$$

and

$$\nabla_{\perp} \cdot (\sigma_{\perp} \nabla_{\perp} \phi') = \nabla_{\perp} \cdot \left[\sigma_{\perp} (\vec{V}_f \times \frac{\vec{B}}{B}) \right]. \quad (40)$$

If we suppose the magnetic field strength to be approximately uniform in the x-y plane, we may divide Eq. (19) through by B and obtain approximately

$$\nabla_{\perp} \cdot \left(\sigma_p \frac{\nabla_{\perp} \phi'}{B} \right) = \nabla_{\perp} \cdot \left[\sigma_p (\vec{V}_f \times \hat{z}) \right] \quad (41)$$

which, for an irrotational neutral wind, becomes

$$\nabla_{\perp} \cdot \left(\sigma_p \frac{\nabla_{\perp} \phi'}{B} \right) = \nabla_{\perp} \sigma_p \cdot (\vec{V}_f \times \hat{z}) = (\nabla_{\perp} \sigma_p \times \vec{V}_f) \cdot \hat{z} \quad (42)$$

where

$$\nabla_{\perp} \phi' = -\vec{E} - \frac{KT_e}{ne} \frac{\nabla n}{n}$$

$$\vec{V}_f = \frac{\vec{G}}{v_n} - \frac{K(T_e + T_i)}{v_n M} \frac{\nabla n}{n}$$

and where \vec{G} is the combined acceleration due to gravity and the neutral wind, as defined after Eq. (8), K is Boltzman's constant, and T_e and T_i are the electron and ion temperatures, respectively.

It is interesting to note that the dynamo current appearing in Eq. (40) contains a substantial diffusion contribution (a "ring current" in the case of axially symmetric irregularities) but that its divergence is zero. Thus, if we take the collision frequency and ion mass to be uniform over distances of interest, so that $\nabla \sigma_p \propto \nabla n$, we obtain no contribution to the final cross product in Eq. (42) from the diffusion term in \vec{V}_f . We are left, then, with

$$\nabla_{\perp} \cdot \left(\sigma_p \frac{\nabla_{\perp} \phi'}{B} \right) = \left(\nabla_{\perp} \sigma_p \times \frac{\vec{G}}{v_n} \right) \cdot \hat{z} \quad (43)$$

Equation (43) is close to the final form of one of the two main MHD equations that constitute the Hele-Shaw analogy, as we shall soon see. Before turning to the cell-fluid equations, however, we must complete our consideration of the plasma velocity. We return, therefore, to Eq. (38), which may be rewritten as

$$\vec{U}_\perp = \frac{(\vec{E} - \frac{M\vec{G}}{e} - \frac{KT_i}{e} \frac{\nabla n}{n}) \times \vec{B}}{B^2} = \left(\frac{\vec{E}}{B} + \frac{\vec{G}}{\omega_c} - \frac{KT_i}{M\omega_c} \frac{\nabla n}{n} \right) \times \hat{z}. \quad (44)$$

To evaluate the relative importance of the three terms in the above expression, we insert some typical values for night-time F-layer parameters (Ratcliffe, 1972: NRL, 1978), as follows:

$$\frac{E}{B} \approx \frac{3 \times 10^{-3} \text{ volts/m}}{0.3 \times 10^{-4} \text{ weber/m}^2} = 100 \text{ m/s}$$

$$\frac{G}{\omega_c} \approx \frac{g}{\omega_c} + \frac{v_n}{\omega_c} \approx \frac{9 \text{ m/s}^2}{250/\text{s}} + (10^{-3})(10^2 \text{ m/s}) = 0.14 \text{ m/s}$$

$$\frac{KT_i}{M\omega_c} \frac{\nabla n}{n} \approx \frac{(1.38 \times 10^{-23} \text{ joule/}^\circ\text{K})(10^3 \text{ }^\circ\text{K})}{(20)(1.67 \times 10^{-27} \text{ kg})(250/\text{s})} \frac{\nabla n}{n} = (1653 \frac{\text{m}^2}{\text{s}}) \frac{\nabla n}{n}.$$

Clearly, for conditions of interest, the cross-field drift produced by the slow gravitational fall and even by the neutral wind (in this low-collision-frequency regime) are negligible compared with the $\vec{E} \times \vec{B}$ drift. More importantly for our present purposes, normal cross-field diffusion may be ignored for gradient lengths down to 100 meters, but not for very sharp gradients.

It is interesting and pertinent to consider in detail the source of the diffusion term in Eq. (44). Appearing in the effective electrostatic potential gradient in the first term of Eq. (38) is a term associated with ambipolar diffusion and arising from the pressure gradient of the electron gas. This term also is included in the left-hand side of Eq. (43). The relationship between this term and the imposed electric field, \vec{E} , must depend on boundary conditions not considered here. A solution for \vec{E} in terms of the boundary conditions and the ambipolar diffusion force, therefore, is relevant to the assessment of limitations on the Hele-Shaw analogue as well as for a full understanding of striation dynamics.

The relevant point for our present purpose is that in the heavy-ion, low-collision approximation appropriate for the simplest Hele-Shaw analogue, the electron-diffusion contributions from the two terms in Eq. (43) cancel, leaving an ion-diffusion contribution to the cross-field drift described by Eq. (44). For an equilibrium plasma ($T_i = T_e$), the upshot

is diffusion terms of equal magnitude but opposite sign in the two equations we need for the analogy. The diffusion contribution to the conduction current contained in parentheses on the left-hand side of Eq. (43), then, may be ignored under the same conditions that the diffusive drift in Eq. (44) may be.

At this juncture, then, we find that we can proceed with the Hele-Shaw analogue without concern about diffusion down to (night-time, F-layer) plasma scales on the order of 100 m. We note that this restriction is quite acceptable for pursuing questions of outer-scale evolution, but the general question of diffusion effects must be regarded as open. Meanwhile, we turn our attention to dynamics of the Hele-Shaw-cell fluid.

We note that a plasma undergoing an $\vec{E} \times \vec{B}$ drift in an approximately uniform magnetic field moves essentially as an incompressible fluid. The cell fluid is incompressible, and since it is undergoing two-dimensional flow, its velocity may be expressed as the curl of a vector potential (Batchelor, 1970) whose only non-zero component is a stream function, $\psi(x,y)$ as follows:

$$\vec{u} = \nabla \times (\psi \hat{z}) \quad (45)$$

$$\text{or } \vec{u} = \nabla \psi \times \hat{z}. \quad (46)$$

But the steady-flow approximation also holds in the cell, so we can solve the Navier-Stokes expression, in the form of Eq. (22b), for the velocity and multiply through by the density to obtain

$$\rho \vec{u}_{\perp} = \frac{d^2}{8\eta} \left(\rho \vec{g}_{\perp} - \nabla_{\perp} p \right) \quad (47)$$

$$\text{so } \nabla \times \rho \vec{u}_{\perp} = \frac{d^2}{8\eta} \left(\nabla_{\perp} \rho \times \vec{g}_{\perp} \right) \quad (48)$$

or, from Eq. (46)

$$\nabla \times (\rho \nabla_{\perp} \psi \times \hat{z}) = \frac{d^2}{8\eta} (\nabla_{\perp} \rho \times \vec{g}_{\perp}) \quad (49)$$

$$\text{or } -\nabla_{\perp} \cdot (\rho \nabla_{\perp} \psi) \hat{z} = \nabla_{\perp} \rho \times \frac{d^2 \vec{g}_{\perp}}{8\eta} \quad (50)$$

where we have ignored effects on the observed gap-center velocity due to the cross-gap gradients of fluid density and velocity. That the velocity is not uniform across the gap is stated by Eq. (18), and it follows that the cross-gap density is not uniform in the fluid-

interchange region. The effects of cross-gap gradients on the dynamics of u_{\perp} on x-y scales significantly larger than d are thought to be innocuous, but this conjecture has not been proven theoretically or experimentally.

C. SUMMARY OF THEORETICAL RESULTS

The first point of analogy between magnetoplasmas and Hele-Shaw fluids is the similarity between the plasma momentum equation and the Navier-Stokes equation as represented by Eqs. (22a and b). The main caveat on the latter is that its drag term depends upon an assumption of zero density gradient across the gap. Related assumptions arise in completing the Hele-Shaw analogue of the magnetoplasma electrodynamics. These and other pertinent assumptions and approximations are identified in Table 1.

Table 1. Pertinent Assumptions and Approximations

<u>Hele-Shaw Fluid</u>	<u>Magnetoplasma</u>
Incompressible	Incompressible
Two-dimensional	$\frac{v}{\omega_c} \ll 1$
No surface tension	$\frac{\nabla_{\perp} B}{B} \ll \frac{\nabla_{\perp} n}{n}$
No capillary action	$\frac{KT}{M\omega_c} \frac{\nabla_{\perp} n}{n} \ll \frac{\nabla_{\perp} \phi}{B}$
$\frac{\nabla^2 \vec{u}_{\perp}}{\vec{u}} \ll d^2$	$\left(\frac{\nabla_{\perp} n}{n} \leq \frac{1}{100m} \right)$
$\frac{\partial p}{\partial z} \approx 0$	$\frac{\nabla n}{n} \gg \frac{\nabla_{\perp} n}{n}$
η uniform	v_{\perp} uniform

We note that the assumption of negligible diffusion in the magnetoplasma restricts application of Hele-Shaw analysis, as presently understood, to plasma scales larger than about 100 m. This is quite acceptable for outer-scale considerations, which are important for assessment and prediction of radiowave scintillation effects.

We now rewrite the central results, Eq. (43), (44), (45), and (50), in light of the approximations summarized in Table 1 and invoke the continuity equations for both the magnetoplasma and the cell fluid to obtain the results in Table 2.

Table 2. Mathematical Analogy

<u>Hele-Shaw Fluid</u>	<u>Magnetoplasma</u>
$\vec{u}_\perp = \nabla_\perp \psi \times \hat{z}$	$U_\perp = \frac{\nabla_\perp \phi}{B} \times \frac{\vec{B}}{B}$
$-\nabla_\perp \cdot \left(\rho \nabla_\perp \psi \right) = \left(\nabla_\perp \rho \times \frac{d^2 \vec{g}_\perp}{8\eta} \right) \cdot \hat{z}$	$-\nabla_\perp \cdot \left(n \frac{\nabla_\perp \phi}{B} \right) = \left(\nabla_\perp n \times \frac{\vec{G}}{v_n} \right) \cdot \frac{\vec{B}}{B}$
$\frac{\partial \rho}{\partial t} + \vec{u}_\perp \cdot \nabla \rho = 0$	$\frac{\partial n}{\partial t} + U_\perp \cdot \nabla n = 0$

We see from the six equations in Table 2 that there is a consistent analogy between (1) the local electrostatic potential, scaled by the magnetic field strength, and the cell-fluid stream function (alternatively between the electric field and the gradient of the stream function); (2) the magnetic field direction and the cross-cell gap direction; (3) the plasma drift velocity and the fluid flow velocity; and (4) the electron number density and the fluid mass density. The key analogy (4) arises from one between the Peterson conductivity and the fluid density, given uniform collision frequency and ion mass (as well as magnetic field strength). The remaining analogous quantities are the effective dynamo velocity, $\frac{\vec{G}}{v_n}$, and the fluid free-fall velocity, $\frac{d^2 \vec{g}}{8}$. Gravity, \vec{g} , in the laboratory plays the role of wind-augmented gravity, \vec{G} , in the field, and the analogy is completed by the drag imposed through the scaled kinematic viscosity, $\frac{8\eta}{d^2}$, in the cell and plasma-neutral collisions, v_n , in the field.

The analogous parameters are summarized in Table 3.

Table 3. Analogous Parameters

<u>Hele-Shaw Fluid</u>	<u>Magnetoplasma</u>
Velocity, \vec{u}_\perp	Velocity, \vec{U}_\perp
Stream function, ψ	Scaled electrostatic potential, $\frac{\phi}{B}$
Cross-gap unit vector, \hat{z}	Field-aligned unit vector, $\frac{\vec{B}}{B}$

$$*\vec{G} = \vec{g} + v_n \vec{V}_\perp$$

Table 3. Analogous Parameters (continued)

Hele-Shaw Fluid

"Free-fall" velocity, $\frac{d^2 \vec{g}_1}{8\eta}$

Mass density, ρ

Magnetoplasma

"Gravitationally assisted"
neutral-wind velocity, $\frac{\vec{G}_1}{v_n}$

N^0 density, n

III. EXPERIMENTAL APPARATUS AND PROCEDURES

A. THE CELL

The mathematical analogy between fluid in a Hele-Shaw cell and a dynamo-convected magnetoplasma is enticing. It offers an opportunity to study, by means of a conceptually simple laboratory device, very complicated dynamic processes otherwise accessible only by means of expensive field experiments and ambitious computations. In practice, however, the experimental procedures are not without their own problems. Certain practical difficulties had been identified in early experiments by Thomson (1971) and by Thomson and Hochstim (1971). Some difficulties were alleviated in a follow-up set of experiments by Ozarski, Piccirelli, and Thomson (1973).

There remained, however, several needs for quantitatively useful experiments. The early experiments had suffered from an inability to maintain a constant gap dimension, d , across the face of the cell, which resulted in nonuniform dynamics via the free-fall driving velocity, $\frac{d \cdot g}{8\eta}$. The follow-up experiments had attempted to solve the problem by means of a small cell, in which the hydrostatic head did not cause the cell to bulge appreciably in the middle. The smallness of the cell, however, limited the horizontal window over which data could be analyzed and the duration of experimental runs permitted by the vertical dimension. Moreover, repeatability of fluid behavior in the early cells had never become truly satisfactory.

In an attempt to realize the promise of the Hele-Shaw technique, a new cell and more controlled laboratory procedures were developed under this contract. A larger cell was designed and built, employing thicker glass for stiffness and mechanically supported for convenient and repeatable initiation of experimental runs; it is illustrated in Figure 1. The overall assembly consists of the cell itself, a frame, a light box, and a floor stand. The cell, proper, consists of two sheets of 3/4-in float glass, cut and ground to overall dimensions of 20 by 50 in. Surface flatness is better than one can measure with a 24-in straightedge and a .0015-in feeler gauge (smoother than 38.1 μm over 61.0 cm).

The cell gap was set at less than a millimeter by means of 0.32-in shim stock, 1 in wide, placed around the perimeter of the glass. The dimensions of the fluid-containing portion of the cell, therefore, are 45.7 cm by 1.22 m by 813 μm (18 by 48 by .032 in). Deformation under hydrostatic load was calculated as 91.4 μm (11% of the gap dimension) at the worst point, and this estimate was confirmed approximately by measurement.



Figure 1. The Helio-Shus cell (white central rectangle) in its frame and pivot mount, showing light box (large off-white rectangle), clocks, and overall size.

The cell, in its frame, is supported by a stand that permits rotation from one vertical orientation (the stable one in which the lighter of the two fluids "floats" on the heavier), used for filling, to the opposite vertical orientation (in which the heavier fluid overlies the lighter), used for experimental runs. A mercury switch mounted on the cell frame initiates a minute and second (to the nearest tenth) counter when the cell is rotated.

Backlighting of the cell fluids is provided by ten 40-watt fluorescent discharge tubes, 48 in long, mounted in a flat-white box that provides an overall illumination field of 48 by 80 in. The lights are mounted horizontally, with the plane of the light source 16 in from the interior glass. Two sheets of 1/8-in translucent plexiglass (Rohm and Nass No. 2447W), placed 10 and 2½ in from the interior glass, are used to diffuse the light.

b. LABORATORY PROCEDURES

Early experimental runs with the cell shown in Figure 1 revealed that control of the cell gap to within 1% by means of thick glass was not sufficient to provide satisfactorily uniform dynamics. A "droop" in the fluid interface, caused by glass bulge, produced two undesirable effects: (1) large-scale convection downward near the middle and upward near the edges of the cell, and (2) more rapid onset of the Rayleigh-Taylor instability near the cell center. The residual glass bulge was compensated for by means of an empirically developed procedure.

We found that release of some fluid from one end of the cell, after filling, with the other end closed to the atmosphere, provided a means for controlling the bulge. The released amount required to provide a straight interface is surprisingly large and quite sensitive to details of the apparatus, but it is also repeatable. Initially, it was found that releasing 90 ml after completely filling the 565-ml cell produced a satisfactory interface. After very minor modifications were made to the filling apparatus (which had the effect of changing the overall hydrostatic head), release of 130 ml was found necessary to produce a straight interface. The latter amount has been found to be consistently satisfactory in the absence of any modifications to the apparatus. Figure 2 shows examples of a Rayleigh-Taylor unstable interface with (right) and without (left) control of the hydrostatic head.

Several fluids have been used for studying hydrodynamic instability in Hele-Shaw cells. The theoretical work of Lord Rayleigh, around the turn of the century, on gravitationally driven instability, and that of Taylor (1950), including an algebraically additive acceleration, led to experiments by Lewis (1950), who employed air/water, air/glycerine, and benzene/water combinations. Saffman and Taylor (1958) addressed the question of instability at a viscosity interface, by means of further experiments employing glycerine and air.

Experiments also have been performed on a water/oil interface for application to petroleum from porous ground. In experiments similar to ours, Wooding (1969) worked with a diffusing interface between the water and a potassium permanganate solution.

Thomson (1970) recognized the mathematical analogy between the dynamics of the Rayleigh-Taylor instability as manifested in a Hele-Shaw cell and the gradient-drift instability in high-altitude plasmas. He noted also the need to maintain the kinematic viscosity constant across the two-fluid interface, in order to simulate the simple ionospheric situation of uniform ion-neutral collision frequency. (It is this same condition - uniform collision frequency - that is violated by a nonuniform interplate gap in the cell.)

For our purposes, we sought two miscible fluids with an appreciable difference in density, ρ , but with essentially identical kinematic viscosity, η , where $\eta = \nu/\nu$ and ν is viscosity. These requirements were approximated by Ozarski, Piccirelli, and Thomson (1973) by using distilled water for the lighter fluid and salt water for the heavier fluid, with glycerine added to each to achieve the required viscosities. We first attempted to repeat their conditions approximately. In order to obtain the maximum density difference, we added sufficient NaCl to fresh water to obtain a saturated salt solution. We then experimented with various combinations of the solution and glycerine and of deionized H₂O and glycerine.

After considerable systematic trial and error, we established a pair of fluids that produced satisfactory kinematic parameters with reasonable consistency. For the light fluid, we employ approximately 64% deionized water and 36% glycerine; the heavy fluid is approximately 70% saturated salt water and 30% glycerine. The kinematic properties are temperature-dependent, so the fluids are measured, readjusted, and measured again for each experimental run. During this iterative process, the heavy fluid is dyed to make it visually and photographically distinguishable from the light fluid. Typically, a difference in density of about 10% is achieved between the dyed, heavy fluid and the clear, light fluid; the difference between their kinematic viscosities is held to about 1%.

The fluid-dyeing process consists of adding a small amount of NaOH to make a basic solution and then introducing a pH indicator, thymol blue. The most difficult experimental parameter to control consistently is the opacity of the dyed fluid. The opacity to white light increases with addition of thymol blue, until a contaminant precipitates out of the fluid. We have not been able to identify fully the conditions that produce precipitation, and it does not appear always to occur at the same optical opacity.

Our procedure is to add thymol blue until a sufficient opacity (subjectively judged on the basis of experience) is reached and to filter out precipitate if necessary. Useful opacity is reached with a mix of about 3½ g of thymol blue to 2 liters of heavy fluid. The



Figure 2. Data frames showing Rayleigh-Taylor unstable fluid interface without counteraction of cell bulge (left) and with counteraction by control of hydrostatic head (right).

filtering process alters the kinematic properties somewhat, so dyeing is an integral part of the iterative preparation of the heavy fluid.

Fluid dyeing is important because relative opacity directly affects the signal-to-noise ratio achieved in photographic recording. We employed a red photographic filter to enhance the contrast between the blue and white-lighted fluids. A series of exposure tests (Fremouw, and Miller, 1980) resulted in selection of 1/125 s at f2.8 with a #25 filter and Tri-X Pan film (ASA 400) as our standard. Early cell runs were developed in Kodak D-76 for 8 minutes at 68°F. Later, development was pushed to 10 minutes, which became our standard.

Some of the exposure-test frames were of the cell in its stable orientation. Micro-densitometer scans vertically across the fluid interface in such a frame were used to define an effective signal-to-noise ratio

$$\frac{S}{N} = \frac{\bar{l} - \bar{h}}{\sigma_l} \quad (51)$$

where \bar{l} is the mean value of film density in the light-fluid portion of the frame, \bar{h} is the mean value in the heavy-fluid portion, and σ_l is the standard deviation of the former. An example of such a scan is shown in Figure 3 (top). The tested frame yielded $S/N \approx 33$ dB. Figure 3 (bottom) contains a horizontal scan across the structured portion of the right-hand data frame in Figure 2. It shows that S/N , as defined in Eq. (51), is not quite achieved in practice, probably because of fluid path-length effects to be discussed in Section IV A.

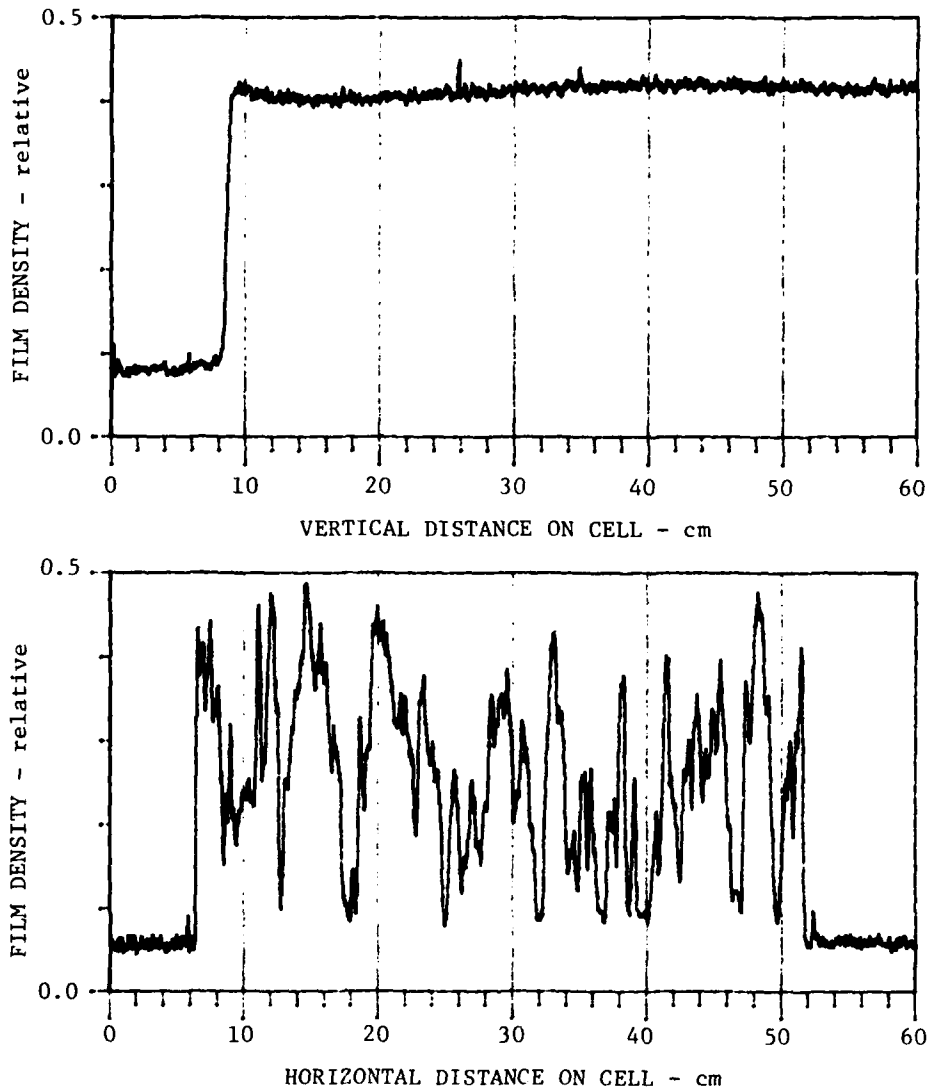


Figure 3. Densitometer scans across stable fluid interface (top) and structured interchange region (bottom).

IV. ANALYSIS PROCEDURES

A. DENSITOMETRY

Figure 4 shows nine data frames exposed during a cell run performed under the standard fluid and photographic conditions described in Section III B. The run, #21, was performed on 10 October 1980 and lasted for just over two minutes. The densities of the heavy and light fluids were 1.207 and 1.103 g/ml, respectively, and the respective kinematic viscosities were 2.46 and 2.50 centistokes.

Data frames such as those shown are scanned with a microdensitometer (Photometric Data Systems Series 1000), the output of which is presented as film density. In principle, the record one wants for analysis is one of fluid density as a function of x-y position on the cell face. If all shades of gray on the film were uniquely related to density levels in the fluid, then the specific relationship between them would be pertinent. In practice, however, we are dealing mainly with two density levels, and we believe that only negligible mixing, due to molecular diffusion, takes place on microscopic scales during the couple of minutes duration of an experimental run.

Intermediate shades of gray do develop during a run, but we believe them to result more from fluid thickness effects than from fluid density. That is, as fingers of the dark and light fluid interpenetrate, a coating of the other fluid originally occupying that portion of the cell is left on the glass surface. Indeed, one would expect such an effect in view of the cross-gap velocity profile described in Eq. (18). Thus, the tips and edges of fluid structures tend to have less contrast than interior portions of the structures having the same centerplane density.

In view of the foregoing complication, there would be little value in trying to identify the quantitative relationship between dye density and mass density in the heavy fluid; for practical purposes, we take them to be proportional. That is, if ρ_h is the mass density of the heavy fluid and ρ_l that of the light fluid and

$$\Delta\rho = \rho_h - \rho_l \tag{52}$$

we suppose the dye density and, therefore, its optical extinction coefficient, to be proportional to $\Delta\rho$.

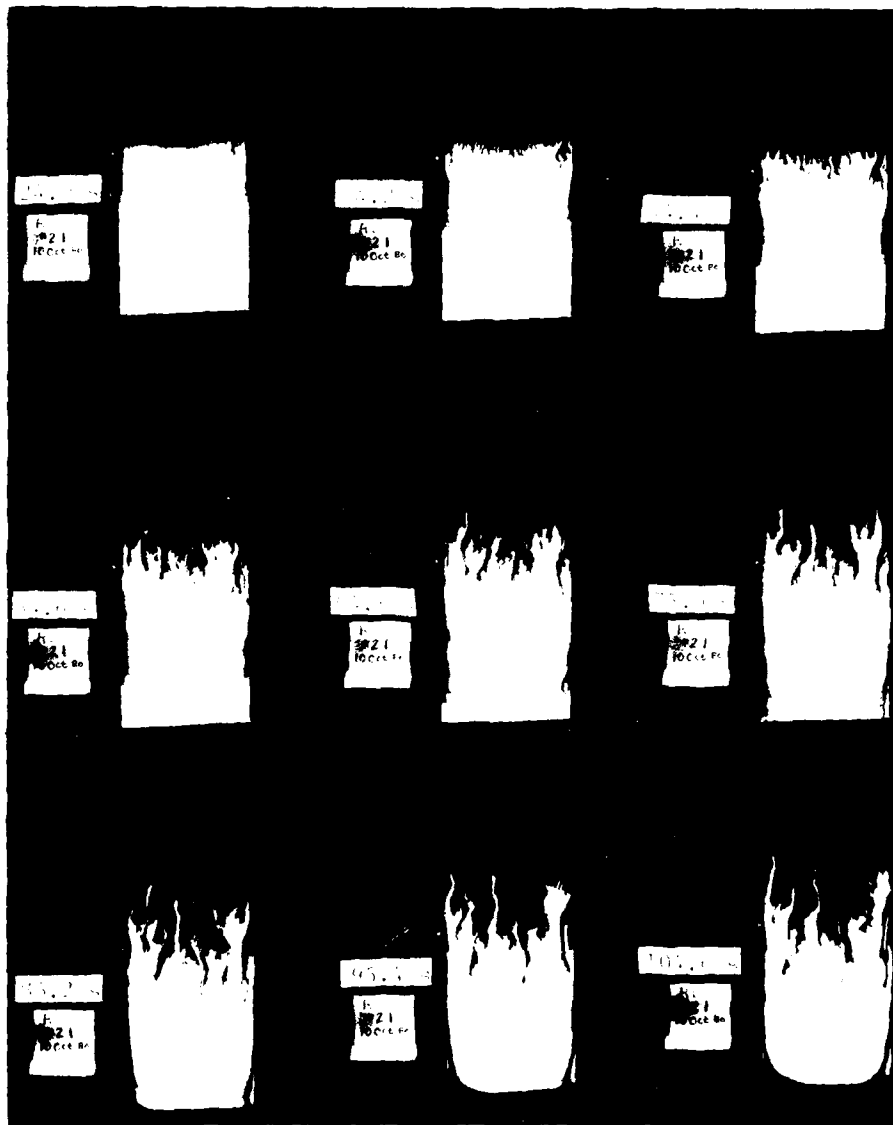


Figure 4. Nine data frames from Run 721, performed 10 October 1980.

Accordingly, the emittance of an elemental surface area in the heavy-fluid portion of the cell is

$$L = L_0 e^{-k\Delta\rho d \sec \theta} \quad (53)$$

and the corresponding photographic exposure is

$$E = E_0 e^{-k\Delta\rho d \sec \theta} \quad (54)$$

where L_0 and E_0 are the emittance and exposure, respectively, of an elemental area on the light-fluid portion of the cell, k is a proportionality constant, d is the cell gap thickness, and θ is the angle between the light ray from the elemental surface area and the central axis of the camera lens. The film density, D , is related to the exposure, E , by properties of the film, a and γ , as follows:

$$D = a + \gamma \log E. \quad (55)$$

From Eqs. (54) and (55), we have

$$D = a + \gamma (\log E_0 - k\Delta\rho d \sec \theta \log e) \quad (56a)$$

$$= b - c \Delta\rho \sec \theta \quad (56b)$$

where b and c are constants given by

$$b = a + \gamma \log E_0$$

and $c = 0.434k$.

Inverting Eq. (28b), we get

$$\Delta\rho = \frac{b-D}{c} \cos \theta \quad (57)$$

where constants b and c are established by the photographic setup and the fluid dye, respectively.

In principle, one could employ Eq. (57) to calculate $\Delta\rho$ to within the constant c . That is, θ could be established from the experiment geometry, and b could be evaluated from the measured film density in the light-fluid portion of a frame. The densitometer record of film density then could be presented as a record of film density in units of (minus) c .

Indeed, one could even adjust the scale factor for different runs to account for the different k (and, therefore, c) values arising from the modest inconsistency in opacity achieved in the dying process. The inconsistency then would affect only S/N and not the signal levels themselves.

Our interest, however, is in behavior of the power spectrum of the density variations, and not in the actual values of fluid density. Our immediate objectives can be met by Fourier transforming the records of film density themselves, and this is what we have done. Figure 5 shows two densitometer scans from run #21.* The upper scan was taken in the y direction across the interface prior to initiation of the Rayleigh-Taylor instability. Referring to Eq. (56), it shows that the constant b was approximately 1.74 film-density units. The gradual drop in film density in the heavy-fluid portion of the scan is attributed to the increasing path length through the translucent, dyed fluid (the $\sec \theta$ trend).

The lower scan in Figure 5 was taken from right to left across the upper portion of the fluid-interchange region (the region in which fingers of light fluid are protruding into heavy fluid) in the third frame (44.4 s) of Figure 4. The zero level at the extreme left and right demarks the non-illuminated cell frame, and the curved baseline level linking them clearly shows the $\sec \theta$ effect. It represents a weak trend on scales considerably larger than that of the structures of interest, and we have not corrected for it. Indeed, its clarity in Figure 5 attests to uniformity of illumination, which was a design objective in the new cell. (The trend variations evident in the top scan of Figure 3 resulted from reflections, which were eliminated later.)

Note, in addition, the difference in film density between the light-fluid portion of the upper scan in Figure 5 and the light-fluid finger tips in the lower scan. As alluded to earlier, this difference is thought to arise from a difference in light-fluid thickness; it decreases the S/N ratio in the interchange region by six dB or so compared with that computed from a scan across the initial interface.

The film employed was in 6 by 4½ cm format, with the result that 1 mm on the cell transforms to 43 μm on the film. Thus, the smallest relevant size on the film, corresponding to the $d = 813 \mu\text{m}$ gap size, is 35 μm . The circular slit used on the densitometer has a diameter of 10.6 μm , which was stepped in overlapping 6- μm steps in the x direction (corresponding to horizontal on the cell). Thus, the densitometer parameters were closely matched to the smallest relevant size, providing about three independent samples in that distance (six sample points on the abscissa of Figure 5).

*Keep in mind that the scans are across negatives of the prints shown in Figure 2.

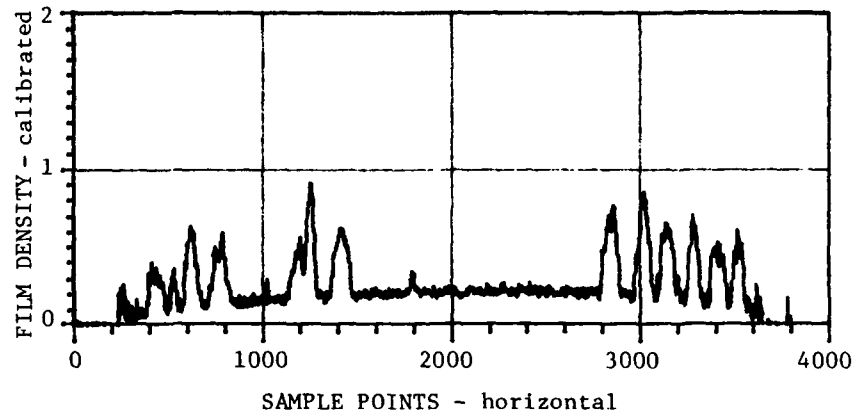
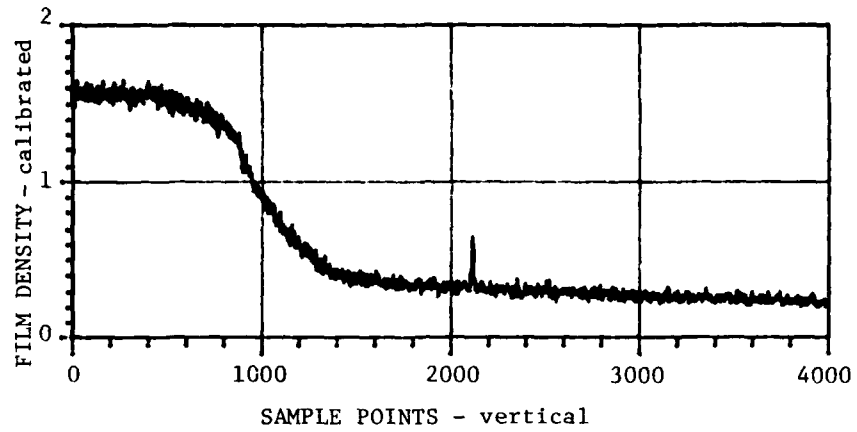


Figure 5. Calibrated densitometer scans across pre-instability interface (top) and upper portion of structured interchange region (bottom) in Run #21.

The film was similarly matched, the response of its modulation transfer function being rated as 80% at 30 cycles/mm (approximately one cycle per imaged gap dimension). Overall, the expected resolution was just slightly coarser than the scale on which third-dimension dynamics might be expected theoretically to produce extraneous effects.

Typically, 50 x-direction densitometer scans were made on a data frame, yielding a scan every 300 μm in the y dimension. Ultimately, two-dimensional statistics (in both configuration and Fourier space) are of interest. Analysis to date, however, has been restricted to the time evolution of one-dimensional statistics in the x direction. In particular, our attention has been focused on development of a one-dimensional outer scale near the original interface between the two fluids.

Densitometer scans from near the middle of the interchange region have been inspected visually to select the one showing most nearly a balance between heavy and light fluid, which is then defined as the center scan for that frame. The center scans for six of the nine frames shown in Figure 2 are presented in Figure 6. The main evolutionary behavior illustrated is an increase in size of the visually dominant structures, to which we shall return in Section V.

Figure 6 also illustrates a problem that has been a source of some difficulty in the present Hele-Shaw experiment: namely, intermittently unreliable operation of the densitometer. When operating properly, the Photometric Systems 1000 has been very suitable for our purpose in terms of resolution, accuracy, and other characteristics. Unfortunately, however, the instrument is old and not fully reliable. It is located at the Boeing Company, from whom we purchased operating time, and Boeing chose not to perform major maintenance on it because of its age and low use rate.

There are two aspects of the densitometer problem: a slowly changing output bias, and variable noise behavior. Both effects are illustrated in Figure 7, which also shows our basis for coping with the former. The figure shows two scans taken across a photographic step tab at different times in a single densitometry session. Comparison clearly shows that the instrument bias and noise-fluctuation levels changed between the scans shown. We have found, fortunately, that the bias drift is slow compared with the time taken to perform densitometry on a single data frame. We have, therefore, been able to calibrate the set of scans from each frame by means of step-tab scans obtained between processing of each pair of data frames. The film density used for display and analysis, may be reliably compared from frame to frame throughout a run because of this calibration procedure. Moreover, response variations from scan to scan are unimportant for analysis, since absolute density is not of concern to us.

More difficult to deal with, however has been the intermittent noise contained on the densitometer records. The noise is enigmatic. Some scans, such as the upper scan in Figure

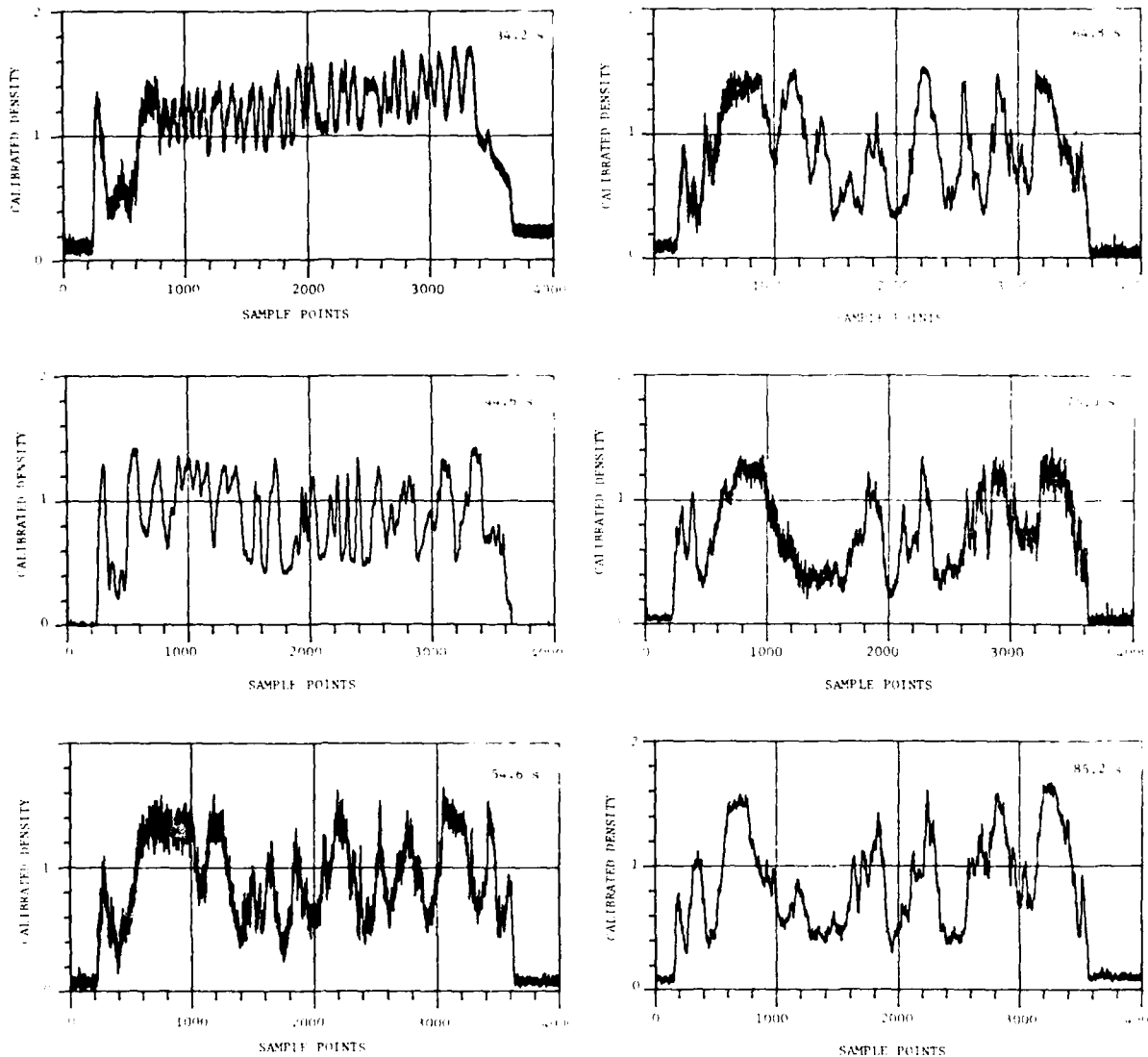


Figure 6. Densitometer scans across the center of the interchange region at 6 times in Run #21.

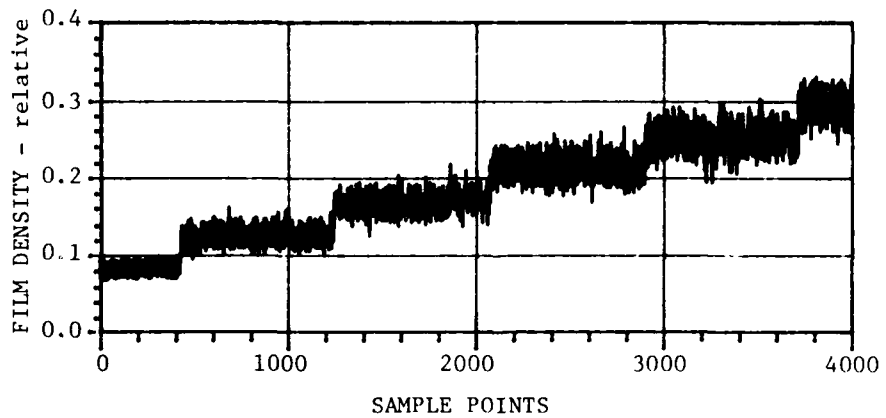
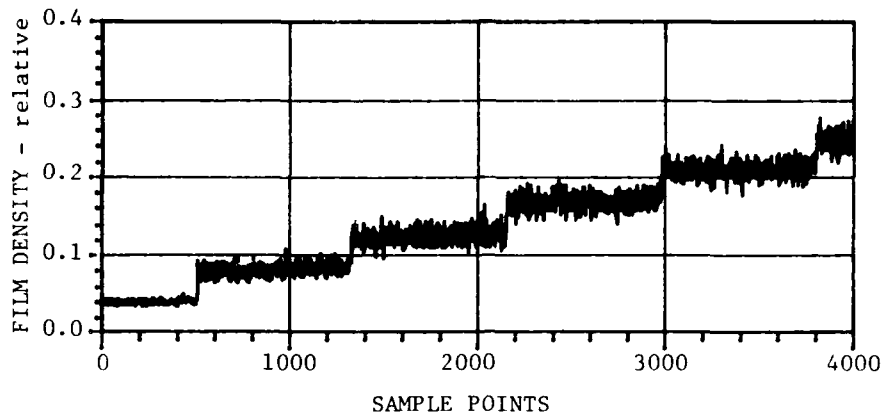


Figure 7. Two densitometer scans across a photographic step tab, showing different bias and noise-fluctuation levels.

7, the second (44.4 s) and last (85.2 s) in Figure 6, and both scans in Figure 5, are free of the added noise. Others, such as the lower scan in Figure 7 and the third (54.6 s) scan in Figure 6, are inundated essentially throughout. Still others, such as the first (34.2 s), fourth (64.8 s), and fifth (75.0 s) in Figure 6, are partly disturbed, sometimes in the same portion of the scan (leftmost portion of the first and fourth).

The scans in Figure 6 are from our most recent densitometer session, and it shows the most seriously degraded data in our collection; the problem is getting worse. Fortunately, the spectral characteristics of the noise experienced have kept it from significantly affecting our outer-scale investigation.

B. SPECTRAL ANALYSIS

Spectra of the six scans appearing in Figure 6 are shown in Figure 8. Our spectral analysis is performed over a processing window of 2028 sample points approximately centered on the cell to avoid edge effects. The spectra in Figure 8 were derived from a window spanning sample points 1000 through 3048 in Figure 6. Inspection of Figure 6 shows that the processing window was essentially free of the spurious noise in the scans from 44.4 s, 64.8 s, and 85.2 s, while the 54.6 s scan was contaminated throughout. Using the 44.4 s scan as a noise-free standard, we see that the main effect of the contamination on the partially affected scans (34.2 s and 75.0 s) is to raise the noise floor at frequencies above about 120 cycles/data window. The effect on the fully contaminated spectrum (54.6 s) is similar in character, but stronger, extending down to perhaps 85 cycles/window. In our outer-scale analysis, we have made use of data only from below the frequency at which noise appears to dominate each spectrum.

In conjunction with our analysis, we investigated the effect of various processing procedures on data obeying a cutoff power-law spectrum (Fremouw, Lansinger, and Miller, 1979). For the investigation, we generated random time series whose power spectral density (PSD) was controlled to be as follows:

$$P(K) = C \left[1 + (LK)^2 \right]^{-n/2} \quad (58)$$

in which the low-frequency power spectral density (PSD), C , the outer scale, L , and the high-frequency spectral index, n , could be controlled. The generation routine also permitted selection of Fourier components that were either synchronous or asynchronous with the processing window and whose phases were either ordered or random.

Our procedure was to generate a time series with selected spectral characteristics and then to process it with the same FFT routine used for analyzing our experimental Hele-Shaw

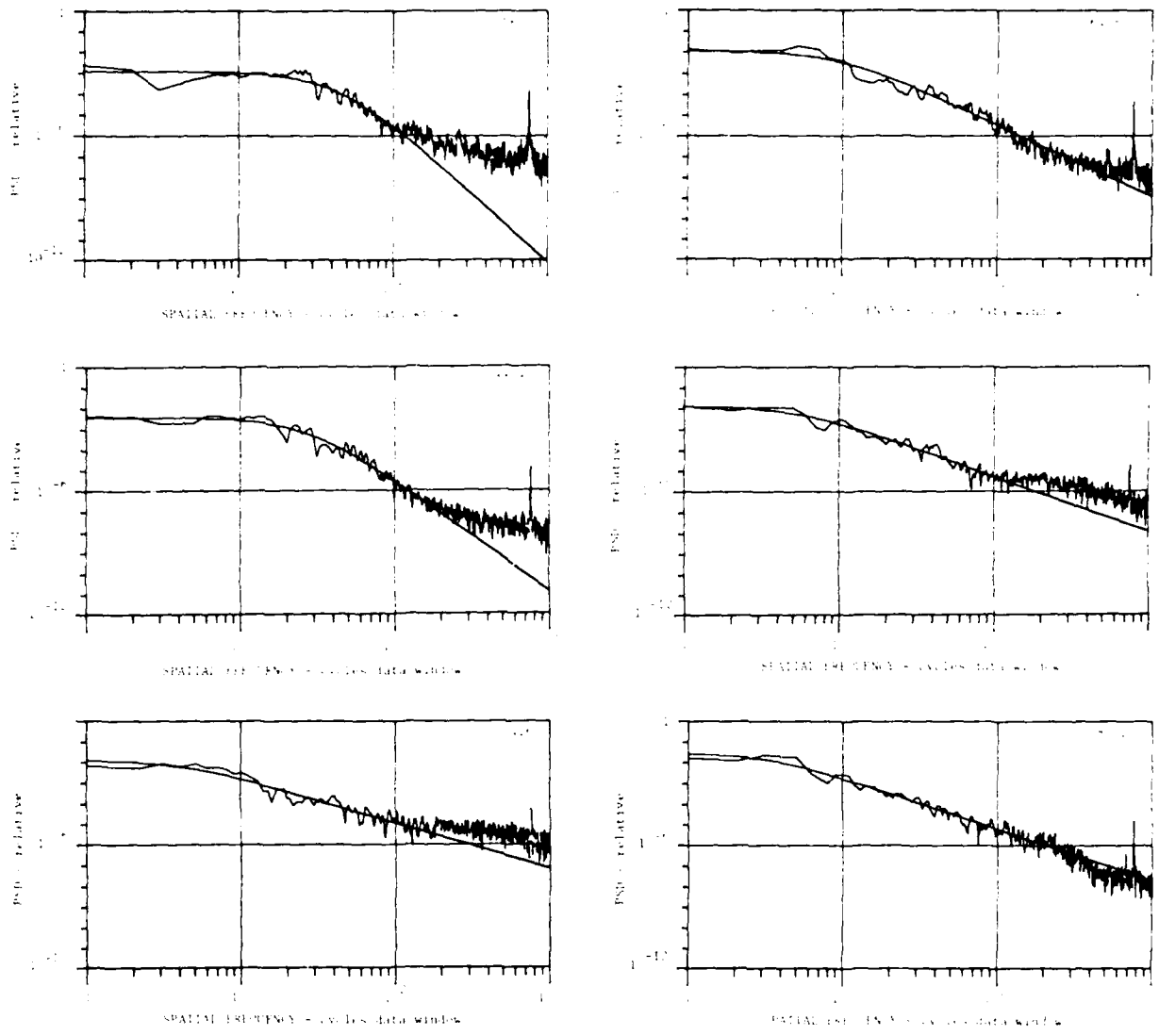


Figure 8. Power spectra of the six densitometer scans shown in Figure 6, together with best-fit analytical spectra of the form given in Eq. (58).

data. The purpose was to assess the relative efficacy of specific analysis procedures, such as windowing with different time-domain tapers, when used to process data for outer-scale studies.

One unexpected, although retrospectively understandable, behavior was noted in preparation for our tests. We found that spectral leakage depends very much on the synchronous/asynchronous nature of spectra, quite independently of the phase relationship between the Fourier components contained. Synchronous data whose spectral lines lie at even half-bins in Fourier space preclude spectral leakage even for a rectangular temporal window because the corresponding spectral window has nulls at such points. Spectral leakage through window sidelobes is maximized by placing the components at odd half-bin frequencies, and we used such tailored synchronous spectra for our window tests.

For our tests, we spectrally analyzed a data set with the foregoing spectral characteristics eight times with different windows. In addition to rectangular, the windows employed (Harris, 1978) were the following: Blackman-Harris with maximum sidelobes down by 61, 67, 74, and 92 dB; and cosine with 10%, 20%, and 30% taper. We then performed three-parameter best fits between the resulting numerical spectra and the analytical spectrum given in Eq. (58). Our concern was the effect of data processing on ascertaining spectral parameters in real data, particularly the outer scale. To test for biases introduced in the curve-fitting procedure, we processed a time series generated from synchronous data tailored for zero, rather than for maximum spectral leakage.

From our test results, we were able to draw three conclusions about processing data that obey a cutoff power-law spectrum. First, choice of an FFT window and of whether to perform spectral smoothing is not of great consequence in identifying relevant spectral parameters, but there are some differences. The best efficacy for evaluation of the outer scale and spectral index was obtained by means of a 30% cosine taper, and we subsequently used such a window in our processing. Second, mean square error is not a very useful indicator of fit-parameter efficacy.

Third, the most important effects revealed in our tests stemmed from the curve-fit procedure, and they can be rendered innocuous by insuring sufficient iterations. If insufficient iterations were employed in our fit procedure, the following consistent biases resulted: spectral strength, C , was too large; spectral index, n , was too small (shallow); and outer scale, L , was too large. The foregoing biases are all understandable for three-parameter fits employing data from the entire spectrum, at least when one fits in logarithmic coordinates. A three-parameter fit routine suitable for use with Eq. (58) and providing sufficient iterations in reasonable time has been developed by McDonald (private communication, 1979), and we employed it for our analysis.

V. RESULTS

In addition to showing experimental PSD's obtained from Hele-Shaw run #21 by means of the spectral analysis described in Section IV B, Figure 8 shows the best fits thereto of Eq. (58). As attested by the smooth curves, the cutoff power-law form provides a very efficacious representation of the experimental spectra. The most striking feature of the experimental PSD's is a consistent transition from a low-frequency white-noise regime to a high-frequency power-law tail. We identify the spectral break with an outer scale and note that it invariably occurs in Hele-Shaw spectra.

Recall that Run #21 employed laboratory fluids carefully controlled to permit relevance of the theoretical development summarized in Section II. Figure 9 shows center-scan spectra and best fits for a run, #7, in which the fluids were not so controlled. The densities of the heavy and light fluids were 1.20 and 1.09, respectively, so the difference of 10% was essentially as in Run #21. While the kinematic viscosities in Run #21 were very nearly equal, however, those in Run #7 were very different (5.6 and 1.8 centistokes for the heavy and light fluids, respectively).

Note now that the general character of the spectra, including the existence of an outer-scale break, is the same for the two runs. Essentially the same instability is responsible for structures that develop at the two-fluid interface in a Hele-Shaw cell whether fluid dissimilarity is dominated by density (Wooding, 1969) or by viscosity (Saffman and Taylor, 1958). It appears, from our results, that the general character of the structural spectrum that develops is quite independent of the specific kinematic properties of the fluids employed.

As we shall soon see, the dynamic evolution of the structure and its spectrum also is qualitatively independent of experimental details, but not quantitatively so. Before proceeding to a discussion of spectral evolution, however, we present one more representative set of center-line scans and spectra.

Figure 10 shows densitometer data obtained from films of Run #44 of the earlier Hele-Shaw experiments performed by Thomson (private communication, 1979). The fluids used for this run were similar to those used for our Run #7, in that the kinematic viscosities of the heavy and light fluids were rather dissimilar, being 6.77 and 2.02 centistokes respectively. The density difference was about 12%, the individual densities being 1.23 and 1.11 gm/l. The cell size was somewhat different from that described in Section III A. The fluid-containing portion measured 61 cm by 46 cm by approximately 1.6 mm, the latter (gap) dimension varying substantially over the cell face.

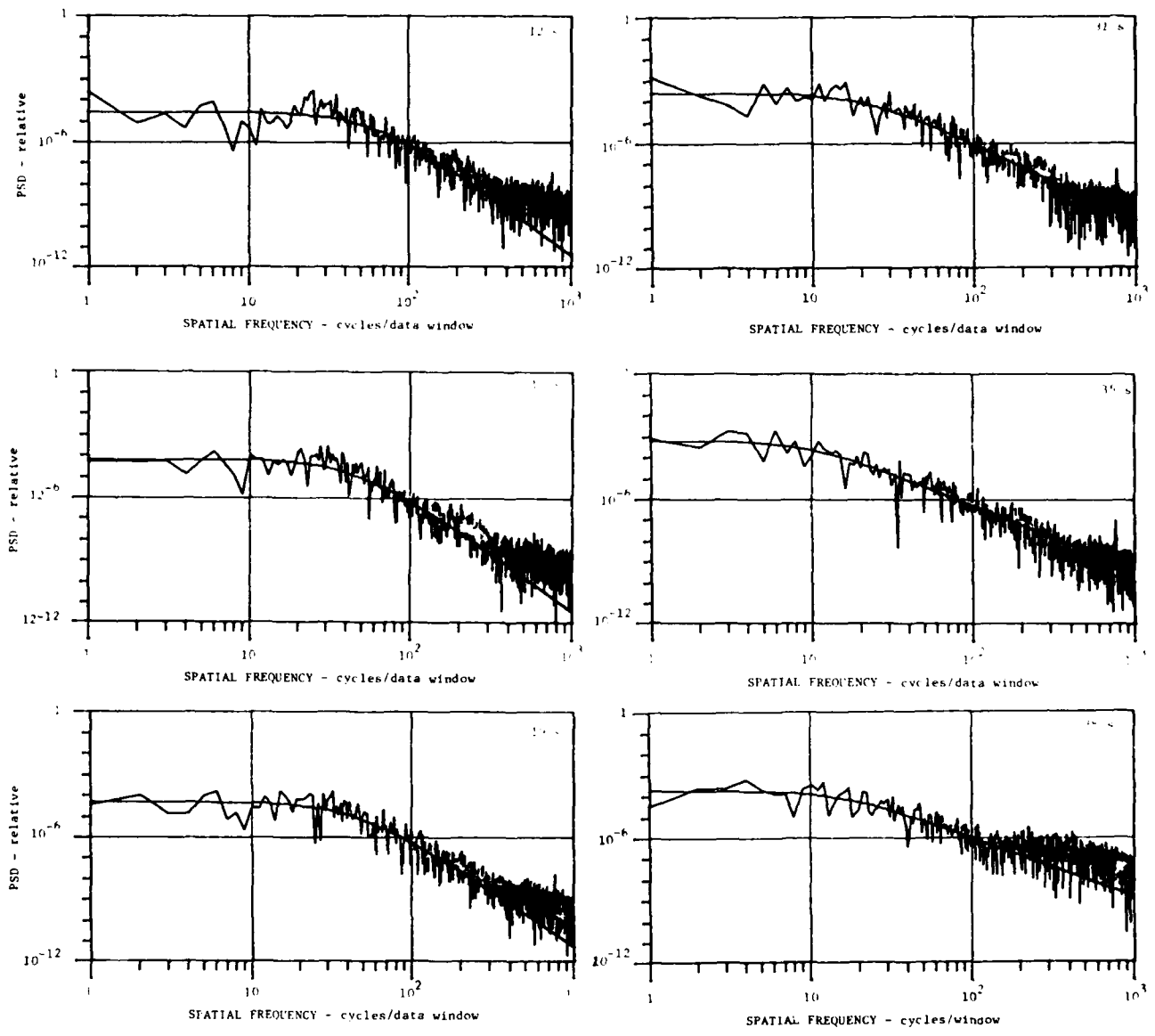


Figure 9. Spectra from six sequential data frames of run #7, each from a scan through the middle of the structured region, and best-fit cutoff power laws.

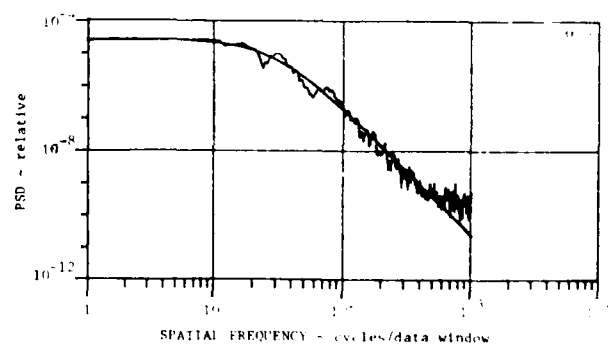
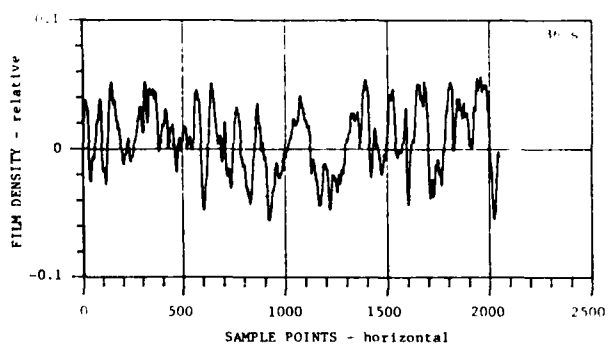
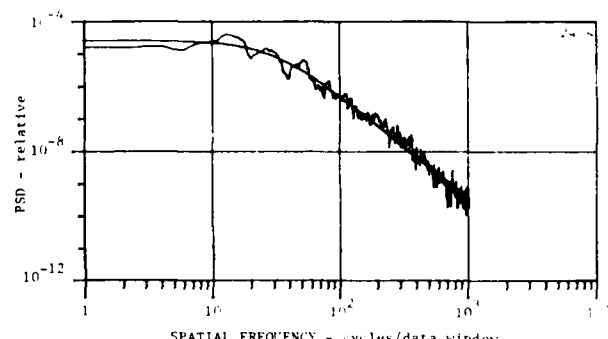
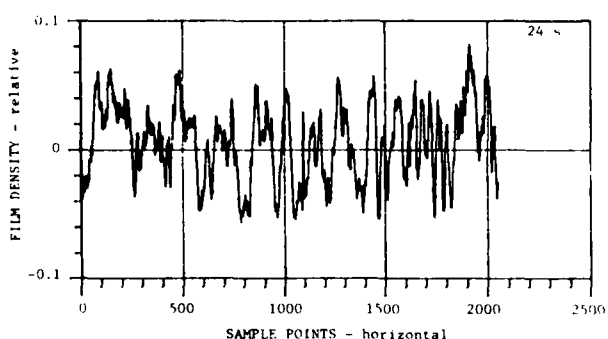
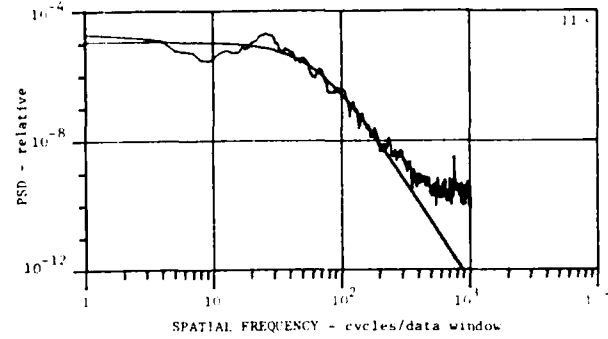
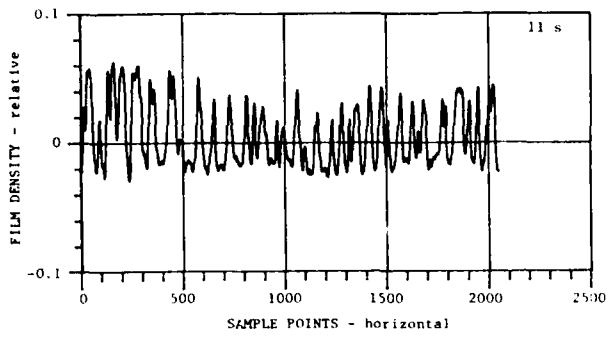


Figure 10. Densitometer scans (left) and corresponding spectra for Hele-Shaw Run #44 by Thomson.

Thomson employed 35-mm film, so the scaling from cell to film is different from that described in Section IIIb. Moreover, in early densitometry, we employed a 46 μ m slit, so the resolution is coarser than in the runs discussed earlier. (The apparently excellent spectral signal-to-noise ratio in Figure 10 stems from a fortuitous matching of the spectral rolloff of the unresolved noise and the underlying data; the spectra are not meaningful beyond about 200 cycles/data window.)

Another difference between the processing of Thomson's Run 44 and that described in Section IV is that detrending had to be included in the former to remove the effects of non-uniform illumination on the cell.* The process employed was developed with considerable care (Fremouw and Miller, 1979), but any detrending raises questions regarding spectral behavior at low frequencies. The similarity of the spectra in Figures 8 and 9, for which detrending was not necessary, to those in Figure 10, for which it was, lends credence to the latter. In particular, the existence of a spectrally identifiable outer scale is very clear.

With an outer scale established, we can move to investigation of its evolution. We have employed the analytical fits shown in Figures 8, 9, and 10 to evaluate the center-line outer scale during the course of the Hele-Shaw runs represented in them. The results are presented in Figure 11 as scatter plots of L , defined in Eq. (58) and scaled in units of distance on the Hele-Shaw cell used in each run, as a function of time.

For the fits, we have employed data from only the portion of the experimental spectrum judged to be reliable and meaningful. For instance, for Run #21, we have used only the bins between 1 cycle/data window and the frequency at which spurious noise is judged to start dominating each spectrum, as discussed in Section IV B. For the noncontaminated spectra from Run #21 and for the other data sets, frequencies between 1 and 180 cycles/data window were used, based on considerations of system resolution and cell-gap size.

For each of the three runs represented in Figure 11, we have superposed a linear least-square trend line. There is considerable scatter in each case, but the sense of the trend is very consistent; outer scale increases with time in all cases. For Run #21, some of the scatter probably results from a residual effect of the spurious densitometer noise. In particular, the third data point (54.6 s) may be erroneously high due to noise effects. Run #7 also contains an outlying point (at 35 s). In this case, there is no suspicion of spurious noise contamination. Rather, the departure of the 35-s point from the trend stems from statistical inhomogeneity in a finite data window. Inspection of the data frame and

*It is detrending that produced essentially zero-centered data scans in Figure 10 as contrasted with Figure 6.

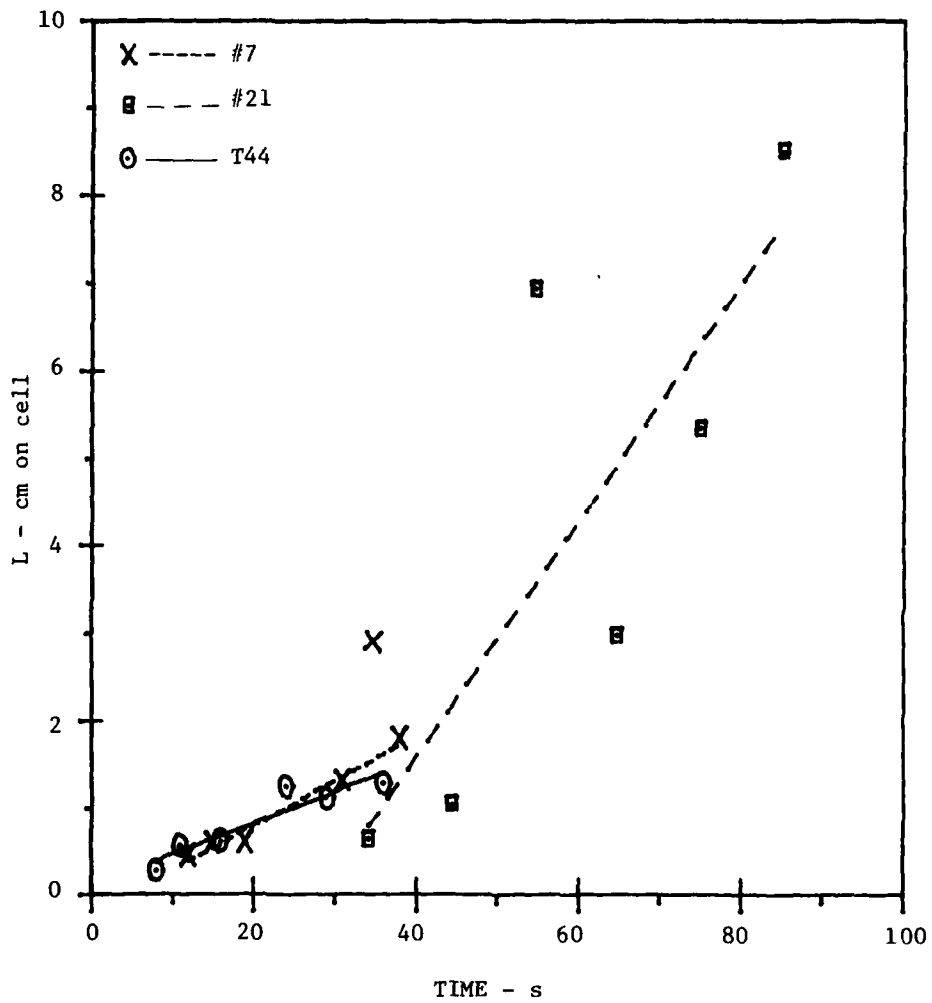


Figure 11. Evolution of the outer scale, L , in our runs #7 and #21 and Thomson's run #44.

densitometer scan in question shows that the spectrum was dominated by two large structures that happened to fall within the processing window. We have excluded the point from the trend fit for Run #7.

The key point to note in Figure 11 is that, despite the point scatter for both experimental and statistical reasons, a clear and consistent trend in outer scale occurred. In all three runs, which were performed under rather different conditions, an outer scale clearly existed and it evolved from smaller to larger size during the course of each experiment.

On the basis of Hele-Shaw data analyzed to date, one could only speculate about the factors controlling the growth of outer scale. We note that for the two runs in Figure 11 for which kinematic viscosity was not held constant for the two fluids, #7 and T44, the growth rate obtained from the best-fit trends in outer scale are rather similar, being 0.5 and 0.4 mm/s respectively. A considerably larger growth rate, 1.4 mm/s, was obtained when the kinematic viscosity was much more controlled for validity of the theoretical analogy, in Run #21.

VI. CONCLUSION

In addition to providing an opportunity for relatively inexpensive quantitative analysis, the Hele-Shaw technique permits two-dimensional visualization of structures developed by the Rayleigh-Taylor instability. One may watch the instability develop in real time, in movie format, and in sequential still photographs.

Except for a few early runs that may be viewed either as experimental "disasters" or as "learning experiences," we have found that the qualitative statistical behavior of the two-fluid interchange in our experiments is repeatable. Moreover, the behavior is consistent with that experienced in the more successful of Thomson's earlier experiments. The qualitative development may be described in terms of the five morphological "stages" identified in Table 4.

Table 4. Observed Morphology

1. First Discernible Structuring -- earliest notable features, usually rising voids;
2. Growth of Reciprocal (Up and Down) Fingers With Increasingly Bulbous Ends and Filamentary Stems -- also, development of lateral warps;
3. Bifurcation and/or Trifurcation of Bulbous Ends;
4. Complicated Growth, including:
 - A. Polyfurcation on stem sides,
 - B. Polyfurcation on bulbous ends,
 - C. Cascading (repeated bifurcation and/or trifurcation of bulbous ends);
5. Increasing Occurrence of Quasi-Pinching and Merging.

Table 4 is ordered chronologically, but the stages are not discrete. Rather, one stage gives way to the next with no clear time of demarcation. Stages 4 and 5 are especially difficult to distinguish from one another, and together they take up a large majority of the duration of a run. Stage 4-5 is dominated by (1) repeated bifurcation and trifurcation at the tips of large-scale fingers of penetrating fluid and (2) simultaneous merging of old structures.

The aforementioned processes (1) and (2) may be viewed as competing for control of the structural spectrum. Their regions of dominance, however, are somewhat distinct. Our quantitative analysis has concentrated on the region near the original fluid interface. Merging dominates in this region, as documented in Section IV. The bulbous tips of the large structures, however, are continuously spawning new, smaller features. In these regions, one

would probably find a rather different one-dimensional spectrum. For instance, horizontal scans near the bottom of the heavy-fluid penetration region reveal clusters of small fingerlets, separated by relatively large voids containing only low-density fluid.

If the foregoing characterization applies to, say, the equatorial F layer, as we believe, then it is clear that a radio wave propagating vertically and scanning horizontally would encounter a variety of local regions with quantitatively different spectral characterizations, as has been suggested by Wittwer (private communication, 1980). It may be that the magnetoplasma spectra are more varied than the cell-fluid spectra. Still, the simple characterization in terms of a cutoff power law, Eq. (58), that we have found so consistently efficacious for the latter can provide very good fits to ionospheric spectra obtained from in-situ probes, as illustrated in Figure 12.

Figure 12 shows an in-situ plasma scan and the corresponding FFT spectrum obtained from Atmospheric Explorer E (Basu and Basu, 1978). The general character of the scan is very similar to that of Hele-Shaw scans, as can be appreciated by comparison with the most noise-free scan (44.5 s) of Figure 6.

In the upper panel of Figure 12, note the spectral break between an essentially white-noise regime and a power-law tail. The solid line superimposed on the measured spectrum represents the best fit by Eq. (58), the parameters of which are $C = 0.6$ fractional electron-density units per km^{-1} , $L = 1.4$ km, and $n = 2.9^*$. Other scans, such as that shown in Figure 12, have been presented by Basu *et al.*, 1979, and we have performed fits to their spectra. In addition to the spectrum from AE-E orbit 7162, shown in Figure 12, we performed fits to two scans from orbit 7048, two from orbit 7049, and one from orbit 7050. The best-fit outer scales obtained were 1.3, 2.0, 1.6, 2.7, and 1.4 km. All but one of these spectra have been published recently by Basu *et al.* (1980).

Our results lead us to conclude that (1) the cutoff power law provides a very suitable spectral representation of both Hele-Shaw-fluid and magnetoplasma data and (2) an effectively finite (smaller than experiment data windows) outer scale can be defined at least locally in time and space. Its spatial homogeneity and temporal evolution are outstanding questions.

We submit that our Hele-Shaw experiments have shed some light on the temporal evolution of the outer scale. Our results, however, are limited in time and space and could be extended in both domains. The logical first step in that extension would be to perform

*We have not assigned any significance to the spectral index, n , of Hele-Shaw data because of uncertainty over the source of shades of gray in the photographs. See Section III B.

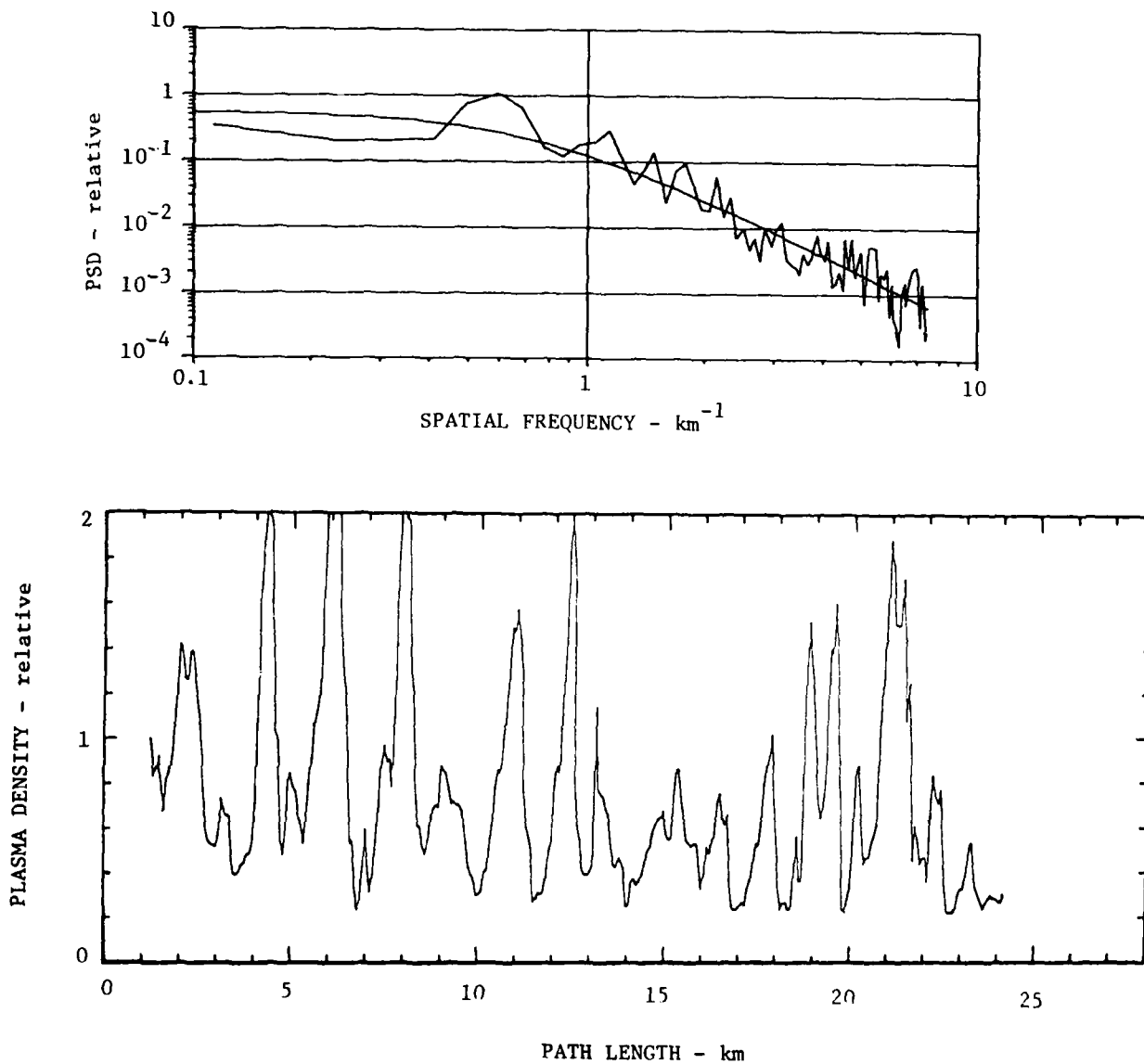


Figure 12. In-situ plasma scan (bottom) and corresponding spectrum (top) obtained in the pre-midnight, bottomside, equatorial F layer (after Basu and Basu, 1978). Smooth curve in top panel is best fit of Eq. (58) to experimental spectrum.

experiments in the existing cell with a different (three-layer) configuration of fluids.

In all of our experiments, the outer scale has continued to increase until the runs have been terminated by fingers reaching the top and bottom of the cell. Wittwer (private communication, 1980) has suggested that the continuous increase in outer scale may result from the effectively infinite reservoir of dissimilar fluids available during the course of a run. He has speculated that a finite reservoir might impose a limit on the outer scale. A test of this conjecture should be possible by means of a relatively narrow layer of heavy fluid sandwiched between two thicker layers of light fluid. It may be that penetration of the heavy layer by rising fingers of light fluid would signal an end to outer-scale growth.

In the closing days of this contract effort, we attempted to produce a three-layer configuration of fluid for such a test. We encountered experimental difficulties in controlling the two interfaces, at least one of which should be totally nonstructured at the outset of the run. As a result, the runs attempted must be classified as "disasters" reminiscent of the "learning experiences" encountered at the beginning of our two-layer experiments. We have little doubt that the experimental difficulties could be overcome by refinement of filling procedures, and we suggest three-layer experiments as a potentially productive endeavor.

Whether with three-layer or resumed two-layer experiments, a second endeavor that also could prove useful would be to explore a locally homogeneous characterization of the spatial spectrum in regions well removed from the initial fluid interface (near the tips of heavy and light fingers). Equally productive, we suggest, would be analytical effort directed at quantitative scaling of Hele-Shaw results to magnetoplasma dynamics, together with experiments designed to probe the control of outer-scale growth rate.

LIST OF REFERENCES

- Basu, Santimay and Sunanda Basu (1978), "*Status Report on Phase Scintillations*," Internal Report on Contract F19628-78-C-0005, Emmanuel College, Boston, June.
- Basu, Santimay, Sunanda Basu, J. Aarons, J. P. McClure, and W. B. Hanson (1979), "*Equatorial Bubbles, Plumes, and Scintillation Patches*," paper delivered at US Fall URSI meeting, Boulder, November.
- Basu, Santimay, J. P. McClure, Sunanda Basu, W. T. Hanson, and J. Aarons (1980) "*Coordinated Study of Equatorial Scintillation and In Situ and Radar Observations of Nighttime F Region Irregularities*," *J. Geophys. Res.*, 85 (A10), pp. 5119-5130.
- Batchelor, G. K. (1970), "*An Introduction to Fluid Dynamics*," Cambridge University Press.
- Fremouw, E. J., J. M. Lansinger and Deborah A. Miller (1979), "*Hele-Shaw-Cell Simulation of Structures in High-Altitude Plasmas*," Bimonthly Progress Report #4 to DNA, Washington, D.C., PD-NW-78-162-RO4, 20 September.
- Fremouw, E. J. and Deborah A. Miller (1979), "*Hele-Shaw-Cell Simulation of Structures in High-Altitude Plasmas*," Bimonthly Progress Report #5 to DNA, Washington, D.C., PD-NW-78-162-RO5, 30 November.
- Fremouw, E. J. and Deborah A. Miller (1980), "*Hele-Shaw-Cell Experiments for Simulation of Structures in High-Altitude Plasmas*," Progress Report #9 to DNA, Washington, D.C., PD-NW-78-162-RO9, 21 July.
- Harris, F. J. (1978), "*On the Use of Windows for Harmonic Analysis with the Discrete Fourier Transform*," *Proc. IEEE*, 66, 55-83.
- Lamb, H. (1945), "*Hydrodynamics*," Dover, N.Y.
- Lewis, D. J. (1950), "*The Instability of Liquid Surfaces When Accelerated in a Direction Perpendicular to their Planes, II*," *Proc. Roy. Soc. A*, 202, pp. 81-96.
- NRL (1970), "*Plasma Formulary*," Naval Research Laboratory, Washington.
- Ozarski, R. G., R. A. Piccirelli, and J. A. L. Thomson (1973), "*Modeling Unstably Stratified Hele-Shaw Flows*," *RIES Report 74-52*, Research Institute for Engineering Sciences, Wayne State University, Detroit.
- Ratcliffe, J. A. (1972), "*An Introduction to the Ionosphere and Magnetosphere*," Cambridge University Press.
- Saffman, P. G. and G. T. Taylor (1958), "*The Penetration of a Fluid into a Porous Medium or Hele-Shaw Cell Containing a More Viscous Liquid*," *Proc. Roy. Soc., A* 245, 312-329.
- Taylor, G. (1950), "*The Instability of Liquid Surfaces When Accelerated in a Direction Perpendicular to Their Planes, I*," *Proc. Roy. Soc. A*, 201, pp. 192-196.

Thomson, J. A. L. (1970), "Quasi-Steady Motions of Weakly Ionized Inhomogeneous Plasma Clouds in a Strong Magnetic Field," in Proceedings of the 1970 SECEDE Summer Study.

Thomson, Alex J. (1971) "A Hydrodynamic Analog of Ionospheric Plasma Releases," PD-71-013, November.

Thomson, J. A. and A. R. Hochstim (1971) "Analysis of Structures in a Hele-Shaw Cell (U)," Physical Dynamics, Inc.

Wooding, R. A. (1969), "Growth of Fingers at an Unstable Diffusing Interface in a Porous Medium or Hele-Shaw Cell," J. Fluid Mech., 39, (3) 477-495.

DISTRIBUTION LIST

DEPARTMENT OF DEFENSE

Assistant Secretary of Defense
Comm, Cmd, Cont & Intell
ATTN: Dir of Intelligence Sys, J. Babcock

Assistant to the Secretary of Defense
Atomic Energy
ATTN: Executive Assistant

Command & Control Technical Center
ATTN: C-312, R. Mason
ATTN: C-650, G. Jones
3 cy ATTN: C-650, W. Heidig

Defense Communications Agency
ATTN: Code 101P
ATTN: Code 480
ATTN: Code 810, J. Barna
ATTN: Code 205
ATTN: Code 480, F. Dieter

Defense Communications Engineer Center
ATTN: Code R123
ATTN: Code R410, N. Jones

Defense Nuclear Agency
ATTN: NAFD
ATTN: NATD
ATTN: STNA
ATTN: RAEE
3 cy ATTN: RAAE
4 cy ATTN: TITL

Defense Technical Information Center
12 cy ATTN: DD

Field Command
Defense Nuclear Agency
ATTN: FCPR

Field Command
Defense Nuclear Agency
Livermore Branch
ATTN: FCPRL

Interservice Nuclear Weapons School
ATTN: TTV

Joint Chiefs of Staff
ATTN: C3S, Evaluation Office
ATTN: C3S

Joint Strat Tgt Planning Staff
ATTN: JLA
ATTN: JLTW-2

National Security Agency
ATTN: B-3, F. Leonard
ATTN: W-32, O. Bartlett
ATTN: R-52, J. Skillman

Defense Intelligence Agency
ATTN: DB, A. Wise
ATTN: DB-4C, E O'Farrell
ATTN: DC-7D, W. Wittin
ATTN: DT-5
ATTN: DT-1B
ATTN: HN-TR, J. Stewart

DEPARTMENT OF DEFENSE (Continued)

Under Secy of Def for Rsch & Engrg
ATTN: Strategic & Space Sys (OS)

WMCCS System Engineering Org
ATTN: J. Hoff

DEPARTMENT OF THE ARMY

Asst Chief of Staff for Automation & Comm
Department of the Army
ATTN: DAAC-ZT, P. Kenny

Atmospheric Sciences Laboratory
U.S. Army Electronics R & D Command
ATTN: DELAS-EO, F. Niles

BMD Advanced Technology Center
Department of the Army
ATTN: ATC-T, M. Capps
ATTN: ATC-O, W. Davies

BMD Systems Command
Department of the Army
2 cy ATTN: BMDSC-HW

Dep Ch of Staff for Ops & Plans
Department of the Army
ATTN: DAMO-ROC

Electronics Tech & Devices Lab
U.S. Army Electronics R & D Command
ATTN: DELET-ER, H. Bomke

Harry Diamond Laboratories
Department of the Army
ATTN: DELHD-N-P, F. Wimenitz
ATTN: DELHD-I-TL, M. Weiner
ATTN: DELHD-N-RB, R. Williams
ATTN: DELHD-N-P

U.S. Army Comm-Elec Engrg Instal Agency
ATTN: CCC-EMEO-PED, G. Lane
ATTN: CCC-CEO-CCO, W. Neuendorf

U.S. Army Communications Command
ATTN: CC-OPS-WR, H. Wilson
ATTN: CC-OPS-W

U.S. Army Communications R & D Command
ATTN: DRDCO-COM-RY, W. Kesselman

U.S. Army Foreign Science & Tech Ctr.
ATTN: DRXST-SD

U.S. Army Materiel Dev & Readiness Cmd
ATTN: DRCLDC, J. Bender

U.S. Army Missile Intelligence Agency
ATTN: J. Gamble

U.S. Army Nuclear & Chemical Agency
ATTN: Library

U.S. Army Satellite Comm Agency
ATTN: Document Control

DEPARTMENT OF THE ARMY (Continued)

U.S. Army TRADOC Sys Analysis Actvy
ATTN: ATAA-TOC
ATTN: ATAA-PI
ATTN: ATAA-TCC, F. Payan, Jr.

DEPARTMENT OF THE NAVY

Joint Cruise Missiles Project Ofc
Department of the Navy
ATTN: JCMG-707

Naval Air Development Center
ATTN: Code 6091, M. Setz

Naval Air Systems Command
ATTN: PMA 271

Naval Electronic Systems Command
ATTN: PME 106-13, T. Griffin
ATTN: PME 117-2013, G. Burnhart
ATTN: PME 117-211, B. Kruder
ATTN: Code 501A
ATTN: PME 106-4, S. Kearney
ATTN: Code 3101, T. Hughes
ATTN: PME 117-20

Naval Intelligence Support Ctr.
ATTN: NISC-50

Naval Ocean Systems Center
ATTN: Code 5322, M. Paulson
ATTN: Code 532, J. Bickel
3 cy ATTN: Code 5324, W. Moler
3 cy ATTN: Code 5532, J. Ferguson

Naval Research Laboratory
ATTN: Code 7500, B. Wald
ATTN: Code 4700, T. Coffey
ATTN: Code 7550, J. Davis
ATTN: Code 4780, S. Ossakow
ATTN: Code 7950, J. Goodman
ATTN: Code 4187

Naval Space Surveillance System
ATTN: J. Burton

Naval Surface Weapons Center
ATTN: Code F31

Naval Telecommunications Command
ATTN: Code 341

Office of Naval Research
ATTN: Code 420
ATTN: Code 465
ATTN: Code 421

Office of the Chief of Naval Operations
ATTN: OP 65
ATTN: OP 981N
ATTN: OP 941D

Strategic Systems Project Office
Department of the Navy
ATTN: NSP-2722, F. Wimberly
ATTN: NSP-2141
ATTN: NSP-43

DEPARTMENT OF THE AIR FORCE (Continued)

Air Force Geophysics Laboratory
ATTN: OPR, H. Gardiner
ATTN: OPR-1
ATTN: LKB, K. Champion
ATTN: OPR, A. Stair
ATTN: S. Basu
ATTN: PHP
ATTN: PHI, J. Buchau
ATTN: R. Thompson

Air Force Weapons Laboratory/
Air Force Systems Command
ATTN: SUL
ATTN: NTYC
ATTN: NTN

Air Force Wright Aeronautical Lab
ATTN: W. Hunt
ATTN: A. Johnson

Air Logistics Command
Department of the Air Force
ATTN: OO-ALC/MM, R. Blackburn

Air University Library
Department of the Air Force
ATTN: AUL-LSE

Air Weather Service, MAC
Department of the Air Force
ATTN: DIXP, R. Babcock

Assistant Chief of Staff
Intelligence
Department of the Air Force
ATTN: INED

Assistant Chief of Staff
Studies & Analyses
Department of the Air Force
ATTN: AF/SASC, C. Rightmeyer
ATTN: AF/SASC, W. Keaus

Ballistic Missile Office
Air Force Systems Command
ATTN: MINXH, J. Allen

Operations Plans and Readiness
Department of the Air Force
ATTN: AFXOKT
ATTN: AFXOKCD
ATTN: AFXOKS
ATTN: AFXOXFD

Research, Development, & Acq
Department of the Air Force
ATTN: AFRDSP
ATTN: AFRDS
ATTN: AFRDSS

Electronic Systems Division
Department of the Air Force
ATTN: DCKC, J. Clark

Aerospace Defense Command
Department of the Air Force
ATTN: DC, T. Long

DEPARTMENT OF THE AIR FORCE (Continued)

Electronic Systems Division
Department of the Air Force
ATTN: XRW, J. Deas

Electronic Systems Division
Department of the Air Force
ATTN: YSEA
ATTN: YSM, J. Kobelski

Foreign Technology Division
Air Force Systems Command
ATTN: NIIS Library
ATTN: TODD, B. Ballard

Headquarters Space Division
Air Force Systems Command
ATTN: SKY, C. Kennedy
ATTN: SKA, D. Bolin

Headquarters Space Division
Air Force Systems Command
ATTN: YZJ, W. Mercer

Headquarters Space Division
Air Force Systems Command
ATTN: E. Butt

Rome Air Development Center
Air Force Systems Command
ATTN: TSLD
ATTN: OCS, V. Coyne

Rome Air Development Center
Air Force Systems Command
ATTN: EEP

Strategic Air Command
Department of the Air Force
ATTN: XPFS
ATTN: DCXT
ATTN: NRT
ATTN: DCXR, T. Jorgensen
ATTN: DCX

OTHER GOVERNMENT AGENCIES

Central Intelligence Agency
ATTN: OSWR/NED

Department of Commerce
National Bureau of Standards
ATTN: Sec Ofc for R. Moore

Department of Commerce
National Oceanic & Atmospheric Admin
ATTN: R. Grubb

Institute for Telecommunications Sciences
National Telecommunications & Info Admin
ATTN: A. Jean
ATTN: L. Berry
ATTN: W. Utlaut

U.S. Coast Guard
Department of Transportation
ATTN: G-DOE-3/TP54, B. Romine

DEPARTMENT OF ENERGY CONTRACTORS

EG&G, Inc.
ATTN: J. Colvin
ATTN: D. Wright

Lawrence Livermore National Lab
ATTN: L-31, R. Hager
ATTN: Technical Info Dept Library
ATTN: L-389, R. Ott

Los Alamos National Scientific Lab
ATTN: D. Simons
ATTN: E. Jones
ATTN: D. Westervelt
ATTN: P. Keaton
ATTN: MS 670, J. Hopkins
ATTN: R. Taschek
ATTN: MS 664, J. Zinn

Sandia National Lab
Livermore Laboratory
ATTN: T. Cook
ATTN: B. Murphey

Sandia National Lab
ATTN: Space Project Div
ATTN: D. Dahlgren
ATTN: Org 1250, W. Brown
ATTN: Org 4241, T. Wright
ATTN: 3141
ATTN: D. Thornbrough

DEPARTMENT OF DEFENSE CONTRACTORS

Aerospace Corp
ATTN: N. Stockwell
ATTN: V. Josephson
ATTN: R. Slaughter
ATTN: D. Olsen
ATTN: I. Garfunkel
ATTN: T. Salmi
ATTN: J. Straus
ATTN: S. Bower

University of Alaska
ATTN: N. Brown
ATTN: T. Davis
ATTN: Technical Library

Analytical Systems Engineering Corp.
ATTN: Radio Sciences

Analytical Systems Engineering Corp.
ATTN: Security

Barry Research Corporation
ATTN: J. McLaughlin

BDM Corp.
ATTN: T. Neighbors
ATTN: L. Jacobs

Berkeley Research Associates, Inc.
ATTN: J. Workman

Betac
ATTN: J. Hirsch

DEPARTMENT OF DEFENSE CONTRACTORS (Continued)

Boeing Co.
ATTN: S. Tashird
ATTN: G. Hall
ATTN: M/S 42-33, J. Kennedy

Booz-Allen & Hamilton, Inc.
ATTN: B. Wilkinson

University of California at San Diego
ATTN: H. Booker

Charles Stark Draper Lab, Inc.
ATTN: D. Cox
ATTN: J. Gilmore

Communications Satellite Corp.
ATTN: D. Fang

Comsat Labs
ATTN: G. Hyde
ATTN: R. Taur

Cornell University
ATTN: M. Kelly
ATTN: D. Farley, Jr.

Electrospace Systems, Inc.
ATTN: H. Logston

ESL, Inc.
ATTN: J. Marshall

General Electric Co.
ATTN: M. Bortner
ATTN: A. Harcar

General Electric Co.
ATTN: C. Zierdt
ATTN: A. Steinmayer

General Electric Co.
ATTN: F. Reibert

General Electric Tech Services Co., Inc.
ATTN: G. Millman

General Research Corp.
ATTN: J. Garbarino
ATTN: J. Ise, Jr.

Horizons Technology, Inc
ATTN: R. Kruger

HSS, Inc.
ATTN: D. Hansen

IBM Corp.
ATTN: F. Ricci

University of Illinois
ATTN: Security Supervisor for K. Yeh

Institute for Defense Analyses
ATTN: J. Bengston
ATTN: J. Aein
ATTN: E. Bauer
ATTN: H. Wolfhard

DEPARTMENT OF DEFENSE CONTRACTORS (Continued)

International Tel & Telegraph Corp.
ATTN: G. Wetmore
ATTN: Technical Library

JAYCOR
ATTN: J. Sperling

JAYCOR
ATTN: J. Doncarlos

Johns Hopkins University
ATTN: T. Pe'emra
ATTN: J. Phillips
ATTN: T. Evans
ATTN: J. Newland
ATTN: P. Komiske

Kaman Tempo
ATTN: W. McNamara
ATTN: T. Stephens
ATTN: M. Stanton
ATTN: W. Knapp
ATTN: DASIAC

Linkabit Corp.
ATTN: I. Jacobs

Litton Systems, Inc.
ATTN: R. Grasty

Lockheed Missiles & Space Co., Inc.
ATTN: R. Johnson
ATTN: M. Walt
ATTN: W. Imhof

Lockheed Missiles & Space Co., Inc.
ATTN: Dept 60-12
ATTN: D. Churchill

M.I.T. Lincoln Lab.
ATTN: D. Towle
ATTN: L. Loughlin

Martin Marietta Corp.
ATTN: R. Heffner

McDonnell Douglas Corp.
ATTN: W. Olson
ATTN: G. Mroz
ATTN: R. Halprin
ATTN: J. Moule
ATTN: N. Harris

Meteor Communications Consultants
ATTN: R. Leader

Mission Research Corp.
ATTN: R. Hendrick
ATTN: F. Fajen
ATTN: D. Sappenfield
ATTN: Tech Library
ATTN: R. Kilb
ATTN: S. Gutsche
ATTN: R. Boqusch

DEPARTMENT OF DEFENSE CONTRACTORS (Continued)

Mitre Corp.
ATTN: B. Adams
ATTN: A. Kymmel
ATTN: G. Harding
ATTN: C. Callahan

Mitre Corp.
ATTN: W. Foster
ATTN: J. Wheeler
ATTN: M. Horrocks
ATTN: W. Hall

Pacific-Sierra Research Corp.
ATTN: F. Thomas
ATTN: E. Field, Jr.
ATTN: H. Brode

Pennsylvania State University
ATTN: Ionospheric Research Lab.

Photometrics, Inc.
ATTN: I. Kofsky

Physical Dynamics, Inc.
10 cy ATTN: E. Fremouw

R & D Associates
ATTN: W. Karzas
ATTN: F. Gilmore
ATTN: B. Gabbard
ATTN: M. Gantsweg
ATTN: C. Greifinger
ATTN: W. Wright
ATTN: R. Turco
ATTN: H. Ory
ATTN: R. Lelevier
ATTN: P. Haas

R & D Associates
ATTN: L. Delaney
ATTN: B. Yoon

Rand Corp.
ATTN: E. Bedrozian
ATTN: C. Crain

Riverside Research Institute
ATTN: V. Trapani

Rockwell International Corp.
ATTN: R. Buckner

Santa Fe Corp.
ATTN: D. Paolucci

DEPARTMENT OF DEFENSE CONTRACTORS (Continued)

Science Applications, Inc.
ATTN: E. Straker
ATTN: D. Hamlin
ATTN: L. Linson
ATTN: C. Smith

Science Applications, Inc.
ATTN: SZ

Science Applications, Inc.
ATTN: J. Cockayne

SRI International
ATTN: G. Smith
ATTN: W. Jaye
ATTN: D. Neilson
ATTN: A. Burns
ATTN: G. Price
ATTN: R. Tsunoda
ATTN: R. Livingston
ATTN: W. Chesnut
ATTN: J. Petrickes
ATTN: R. Leadabrand
ATTN: C. Rino
ATTN: M. Baron

Sylvania Systems Group
ATTN: M. Cross

Technology International Corp.
ATTN: W. Boquist

Tri-Com, Inc.
ATTN: D. Murray

TRW Defense & Space Sys Group
ATTN: R. Plebuch
ATTN: D. Dee

Utah State University
ATTN: K. Baker
ATTN: J. Dupnik
ATTN: L. Jensen

Visidyne, Inc.
ATTN: J. Carpenter
ATTN: C. Humphrey

Rockwell International Corp.
ATTN: S. Quilici

**N
DATE
ILME**